CANCER IMMUNOLOGY

Expansion of tumor-reactive CD8$^+$ T cell clonotypes occurs in the spleen in response to immune checkpoint blockade

Duncan M. Morgan[1,2]†, Brendan L. Horton[2]†‡, Vidit Bhandarkar[2,3]†, Richard Van[2,3], Teresa Dinter[2,3], Maria Zagorulya[2,3], J. Christopher Love[1,2], Stefani Spranger[2,3]*

Immune checkpoint blockade (ICB) enhances T cell responses against cancer, leading to long-term survival in a fraction of patients. CD8$^+$ T cell differentiation in response to chronic antigen stimulation is highly complex, and it remains unclear precisely which T cell differentiation states at which anatomic sites are critical for the response to ICB. We identified an intermediate-exhausted population in the white pulp of the spleen that underwent substantial expansion in response to ICB and gave rise to tumor-infiltrating clonotypes. Increased systemic antigen redirected differentiation of this population toward a more circulatory exhausted KLR state, whereas a lack of cross-presented tumor antigen reduced its differentiation in the spleen. An analogous population of exhausted KLR CD8$^+$ T cells in human blood samples exhibited diminished tumor-trafficking ability. Collectively, our data demonstrate the critical role of antigen density within the spleen for the differentiation and expansion of T cell clonotypes in response to ICB.

INTRODUCTION

Immune checkpoint blockade (ICB) using antagonist antibodies targeting CTLA-4 or PD-1/PD-L1 can provide durable responses against cancer for a subset of patients (*1*). Understanding the mechanisms of response to ICB could improve the selection of patients and the development of new therapies. Most evidence suggests that ICB enhances the functionality of tumor-reactive CD8$^+$ T cells (*2*–*4*). An antitumor CD8$^+$ T cell response is a sequential, multistep process involving the coordination of a variety of cell types across multiple anatomic locations (*5*). This process initiates with the priming of naïve CD8$^+$ T cells by dendritic cells (DCs) in the tumor-draining lymph node (TdLN) (*6*, *7*). Tumor-reactive CD8$^+$ T cells then undergo clonal expansion and differentiate into T cells with effector functions (*8*, *9*), followed by migration to the tumor, where they eliminate tumor cells (*10*). Tumors use immunosuppressive mechanisms to avoid engagement from cytotoxic T cells (*11*), including chronic expression of tumor antigens, which induces exhaustion among tumor-reactive CD8$^+$ T cells (*12*, *13*). Exhausted CD8$^+$ T cells express elevated levels of inhibitory checkpoint receptors that reduce T cell functionality (*14*). Blocking these receptors with ICB can increase T cell responsiveness to other costimulatory signals (*14*, *15*), promote clonal expansion of functional CD8$^+$ effector T cells (*16*), and enhance migration of CD8$^+$ effector T cells to the tumor, reinvigorating the antitumor immune response.

Recent studies have demonstrated that T cell exhaustion represents a distinct trajectory of differentiation (*17*–*21*). An exhausted CD8$^+$ T cell response comprises heterogenous differentiation states, including TCF-1$^+$ "stem-like" progenitor-exhausted T cells (*17*–*21*), which exhibit an enhanced ability to respond to ICB (*22*, *23*). TCF-1$^+$ CD8$^+$ T cells are critical for ICB responses, but the anatomic locations from which these ICB-responsive CD8$^+$ T cells emerge are unclear (*24*–*28*). TdLNs and tumors have been proposed as sites that maintain ICB-responsive CD8$^+$ T cell populations (*24*–*28*), but peripheral expansion also appears critical for generating reinvigorated tumor-infiltrating CD8$^+$ T cells (*29*–*31*). Transcriptional analyses of lymphocytic choriomeningitis virus (LCMV)–specific CD8$^+$ T cells have highlighted additional transcriptional states associated with exhaustion, including intermediate-exhausted populations (*32*, *33*). Nonetheless, the precise transcriptional states of T cells providing tumor control in response to ICB and the anatomic locations from which responses to ICB emerge remain unclear.

Using paired single-cell RNA (scRNA) and T cell receptor (TCR) sequencing, we profiled endogenous, tumor-reactive T cells isolated from tumors, TdLNs, and spleens of mice treated with ICB. We found that the spleen was a critical anatomic site for coordinating the differentiation of an intermediate-exhausted CD8$^+$ T cell population into either a terminally exhausted phenotype, which comprised most tumor-infiltrating cells, or into an exhausted killer cell lectin-like receptor (KLR) phenotype that was rarely found in the tumor. Increasing systemic antigen enhanced the differentiation of this splenic intermediate population toward the blood-resident exhausted KLR phenotype, leading to reduced numbers of tumor-infiltrating T cells in untreated mice. The expansion and differentiation of splenic intermediate-exhausted T cells in response to ICB was dependent on cross-presenting DCs. This suggests that differentiation of CD8$^+$ T cells is affected by both tissue site and antigen level. Using human datasets, we observed the exhausted KLR transcriptional state in blood and determined that this differentiation state displayed limited infiltration into tumors, despite clonal expansion. These results demonstrate that antigen-specific restimulation in the spleen is required for the expansion of tumor-infiltrating clonotypes in response to ICB and that increasing levels of systemic antigen perturb the differentiation of these clonotypes to favor the exhausted KLR state, thereby blunting tumor infiltration.

[1]Department of Chemical Engineering, MIT, Cambridge, MA 02139, USA. [2]Koch Institute at MIT, Cambridge, MA 02139, USA. [3]Department of Biology, MIT, Cambridge, MA 02139, USA.
*Corresponding author. Email: spranger@mit.edu
†These authors contributed equally to this work.
‡Deceased.

RESULTS

Tumor-reactive CD8$^+$ T cells accumulate in the spleen during ICB

To establish the impact of ICB on tumor growth, we inoculated mice subcutaneously with KP lung cancer cells and treated the mice with ICB (Fig. 1A). Consistent with our previous report (*9*), ICB delayed the growth of subcutaneous KP tumors (Fig. 1B). To track tumor-reactive CD8$^+$ T cells, we used a KP cell line engineered to express the model antigen SIY, which binds H2-K^b (KP.SIY). KP.SIY tumor growth was also delayed by ICB, with treated tumors displaying a reduced size at day 14 after implantation (fig. S1, A and B, and Fig. 1, C and D). At this time point, we observed an increase in the absolute number and frequency of SIY-reactive CD8$^+$ T cells in the spleens of mice after ICB (Fig. 1, E to G, and fig. S1C). The specificity of the SIY-reactive tetramer was validated, and tetramer-positive cells were CD44$^+$ (fig. S1, D to G). To assess the generalizability of our findings, we also profiled SIY-reactive CD8$^+$ T cells isolated from TdLNs, spleens, and tumors from two additional tumor models, MC38.SIY and LL/2.SIY. Similar to the KP.SIY model, nearly all SIY-reactive T cells were CD44$^+$ (fig. S2, A and B), and we observed a strong accumulation of SIY-reactive T cells in the spleen after ICB (fig. S2, C to H).

We observed a similar expansion profile between splenic and blood-derived T cells (fig. S2I and Fig. 1G), which could reflect

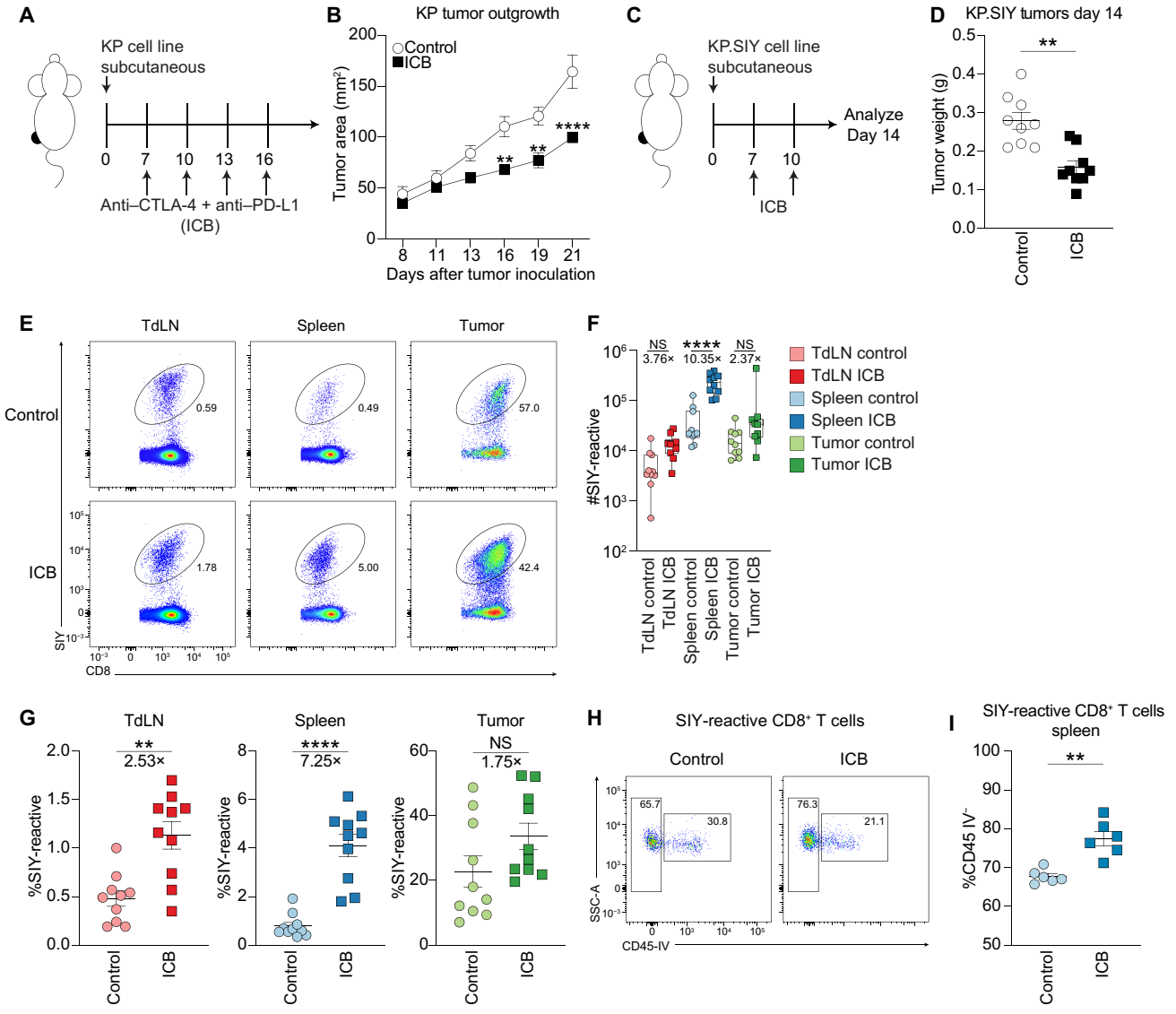

Fig. 1. Tumor-reactive CD8$^+$ T cells accumulate in the white pulp of the spleens of ICB-treated mice. (**A**) ICB treatment scheme of mice bearing subcutaneous KP tumors. (**B**) KP flank tumor outgrowth; $n = 6$; P values calculated using two-way ANOVA. (**C**) ICB treatment scheme of mice bearing subcutaneous KP.SIY tumors. (**D**) Weight of day 14 KP.SIY tumors; $n = 9$; P values calculated with a Mann-Whitney U test. (**E**) Representative staining of SIY-reactive CD8$^+$ T cells in TdLN, spleen, and tumor on day 14. (**F**) Number of SIY-reactive CD8$^+$ T cells in TdLN, spleen (white pulp), and tumor on day 14. Fold changes were calculated using the median value from each condition; $n = 10$; P values calculated with one-way ANOVA. (**G**) Percent of CD8$^+$ T cells that are SIY-reactive in TdLN, spleen (white pulp), and tumor. Fold changes were calculated using the median value from each condition; $n = 10$; P values calculated with a Mann-Whitney U test. (**H** and **I**) Representative staining (H) and quantification (I) of the percentage of SIY-reactive CD8$^+$ T cells in the white pulp (CD45-IV$^-$ fraction) of the spleen, $n = 6$. P values were calculated with a Mann-Whitney U test. NS, not significant.

expanded splenic T cells reentering circulation or active expansion in the blood. To consider these possibilities, we distinguished $CD8^+$ T cells in the white pulp and red pulp of the spleen by intravenously (IV) administered fluorescently labeled anti-CD45 antibody 3 min before euthanasia (fig. S2, J and K). We observed a much greater expansion of SIY-reactive $CD8^+$ T cells after ICB in the white pulp ($CD45\text{-}IV^-$) (8.8×) compared with a more modest expansion in the red pulp ($CD45\text{-}IV^+$) (4.4×) (fig. S2L). Moreover, we found that 73.2% of splenic SIY-reactive $CD8^+$ T cells in control mice were located in the white pulp and that this fraction increased to 82.6% after ICB treatment (Fig. 1, H and I). This observation suggests that SIY-reactive $CD8^+$ T cells preferentially expand in the white pulp of the spleen.

Transcriptional states present among tumor-reactive $CD8^+$ T cells comprise the full spectrum of T cell exhaustion

To determine the phenotypic and clonotypic features underlying the distinct expansion potential of SIY-reactive T cells in the white pulp of the spleen, we performed scRNA and TCR sequencing of endogenous SIY-reactive T cells from the tumors, TdLNs, and white pulp of five untreated and five ICB-treated KP.SIY tumor–bearing mice (Fig. 2A) (*34*). After exclusion of naïve-like and low-quality single cells (fig. S3, A to F), we performed Uniform Manifold Approximation and Projection (UMAP) for dimensionality reduction and identified 10 distinct transcriptional states using unsupervised Louvain clustering (Fig. 2, B and C).

To identify how these transcriptional states related to the trajectory of T cell exhaustion, we generated gene expression signatures using two single-cell atlases of $CD8^+$ T cell transcriptional phenotypes in chronic LCMV infection (*32*, *33*) and overlaid the phenotypic signatures onto our data (Fig. 2, D and E). In our data, we identified one cluster of precursor-exhausted T cells, one cluster of progenitor-exhausted T cells, two clusters of intermediate-exhausted T cells, two clusters of terminally exhausted T cells, one cluster of exhausted KLR T cells, one cluster that up-regulated transcripts associated with interferon response, and two clusters of proliferating T cells (Fig. 2, B and C). Consistent with these annotations, precursor- and progenitor-exhausted T cells expressed high levels of the transcript *Slamf6* (Fig. 2C). Precursor-exhausted T cells were highly proliferative, up-regulated transcripts associated with translation and protein synthesis, and down-regulated *Btg1*, whereas progenitor-exhausted T cells expressed higher levels of the transcription factor *Tcf7* (Fig. 2, C and F). Intermediate-exhausted T cells expressed elevated levels of transcripts associated with tissue homing (*Ccr2*, *Cxcr6*, and *Itgax*) and effector function (*Gzma* and *Gzmb*) and down-regulated *Sell* and *Tcf7* (Fig. 2, C and G). Among the two states of intermediate-exhausted T cells, intermediate 2 T cells up-regulated transcripts such as *Itgae* and *Ccr10*, suggesting that they might comprise precursors of tissue-resident memory T cells (*35*, *36*). Conversely, the intermediate 1 T cells up-regulated transcripts such as *Itga4*, *Gzmk*, and *Eomes*, consistent with tissue-homing effector T cells (fig. S3G). Terminally exhausted T cells up-regulated transcripts such as *Lag3*, *Tnfrsf9*, and *Cd69* (Fig. 2, C and H). Among terminally exhausted T cells, exhausted 1 T cells expressed transcripts associated with cytokine signaling (*Ifngr1* and *Il12rb2*), whereas exhausted KLR T cells up-regulated transcripts encoding KLRs (*Klrg1, Klrk1*) as well as *Cx3cr1* (fig. S3, H to J). Last, interferon-responsive T cells up-regulated a variety of transcripts associated with interferon sensing (fig. S3K).

To annotate the remaining two states of proliferating T cells, we performed label transfer of cluster identities from nonproliferating to proliferating T cells (Fig. 2I). These results demonstrated that most proliferating T cells had transcriptional states consistent with either a $Cxcr3^+$ intermediate 1 phenotype or a $Slamf6^+$ progenitor-exhausted phenotype. In sum, these results demonstrate that the transcriptional phenotypes present in this tumor model recapitulate the full spectrum of transcriptional phenotypes that have been observed in models of chronic viral infection in mice (*32*, *33*).

States of T cell exhaustion vary in frequency among the tumor, lymph node, and spleen

We next examined the frequency of each transcriptional phenotype among the recovered SIY-reactive $CD8^+$ T cells from the tumor, TdLN, and white pulp (Fig. 3A and fig. S4A). In control and ICB-treated mice, the TdLN was enriched in transcriptional states associated with early stages of T cell exhaustion, including precursor T cells and progenitor T cells. In contrast, the white pulp contained elevated frequencies of intermediate-exhausted T cell states, and the tumor comprised T cells with terminally exhausted phenotypes. These data suggest that the TdLN, spleen, and tumor are populated by increasingly differentiated phenotypes of tumor-reactive $CD8^+$ T cells, highlighting a spatially resolved trajectory of T cell differentiation.

We also examined the impact of ICB treatment on the frequency of specific transcriptional states across all three tissues (Fig. 3B). ICB resulted in the expansion of intermediate 1 T cells, but not intermediate 2 T cells, in both the spleen and TdLN. Regardless of ICB treatment, T cells in tumors remained almost entirely within the exhausted 1 phenotype, whereas exhausted KLR T cells were found predominantly in the white pulp and were largely absent from any other anatomic locations.

We established a lymphoid tissue–specific gating strategy for flow cytometry to distinguish among progenitor, intermediate 1, and exhausted KLR T cells, which comprised most SIY-reactive $CD8^+$ T cells in the white pulp and TdLN. *Cxcr3* and *Cx3cr1* transcripts were differentially expressed among progenitor, intermediate 1, and exhausted KLR T cell populations (fig. S4, B and C, and Fig. 3C). Using flow cytometry, we confirmed the presence of a $CXCR3^+CX3CR1^+$ population, consistent with an intermediate 1 phenotype, and a $CXCR3^-CX3CR1^+$ population, consistent with an exhausted KLR phenotype, in the white pulp of tumor-bearing mice (Fig. 3D). To validate that these protein markers identify T cells with intermediate 1 and exhausted KLR transcriptional phenotypes, we performed bulk RNA sequencing of sorted splenic $CXCR3^+CX3CR1^+$ and $CXCR3^-CX3CR1^+$ SIY-reactive T cells. We observed a high degree of concordance among transcripts differentially expressed by these sorted populations and the intermediate 1 and exhausted KLR populations in our single-cell data (fig. S4, D to F), suggesting that CXCR3 and CX3CR1 can be used to distinguish between these two transcriptional phenotypes.

We next assessed the frequency of $CXCR3^+CX3CR1^-$ progenitor T cells, $CXCR3^+CX3CR1^+$ intermediate 1 T cells, and $CXCR3^-CX3CR1^+$ exhausted KLR T cells in control and ICB-treated mice. Consistent with our scRNA sequencing (scRNA-seq) results, we observed an increase in the frequency and number of $CXCR3^+CX3CR1^+$ intermediate 1 T cells in both the TdLN and white pulp after ICB treatment (Fig. 3E and fig. S5, A and B). The frequency of $CXCR3^+CX3CR1^+$ intermediate 1 T cells was highest in the white pulp, both in

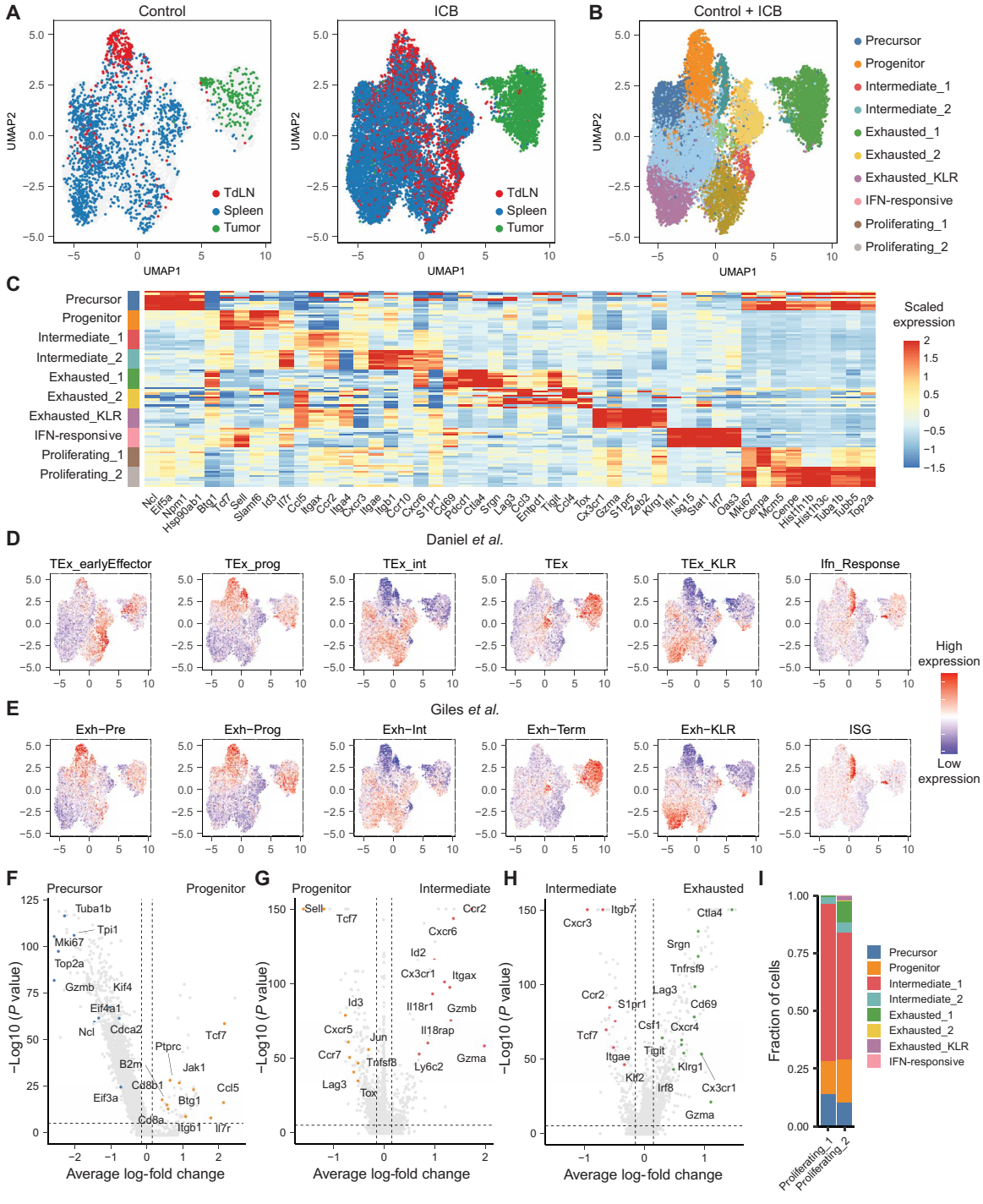

Fig. 2. Single-cell, multitissue transcriptional atlas of SIY-reactive CD8$^+$ T cells. (**A**) UMAP of SIY-reactive CD8$^+$ T cells from untreated or ICB-treated KP tumor–bearing mice recovered colored by tissue [$n = 5$ untreated mice (hashed and pooled), $n = 5$ ICB-treated mice (hashed and pooled)]. (**B**) UMAP of SIY-reactive CD8$^+$ T cells colored by phenotype. (**C**) Heatmap of scaled gene expression of marker genes in SIY-reactive CD8$^+$ T cell phenotypes. Each row represents cells from one phenotype recovered from an individual mouse. (**D**) UMAP of gene expression signatures defined among splenic gp33-reactive CD8$^+$ T cells recovered from day 21 of clone 13 LCMV infection by Daniel *et al.* (*33*). (**E**) UMAP of gene expression signatures defined among splenic gp33-reactive CD8$^+$ T cells recovered from days 15 and 30 of clone 13 LCMV infection by Giles *et al.* (*32*, *60*). (**F**) Volcano plot of transcripts differentially expressed between precursor-exhausted T cells and progenitor-exhausted T cells. (**G**) Volcano plot of transcripts differentially expressed between intermediate-exhausted T cells (intermediate 1 and intermediate 2) and progenitor-exhausted T cells. (**H**) Volcano plot of transcripts differentially expressed between terminally exhausted T cells (exhausted 1, exhausted 2, and exhausted KLR) and intermediate-exhausted T cells (intermediate 1 and intermediate 2). (**I**) Label transfer of nonproliferating T cell phenotypes onto proliferating phenotypes. *P* values for volcano plots were calculated using a two-sided Wilcoxon rank sum test and were adjusted using Bonferroni correction. Genes with an average log-fold change >0.25 and an adjusted *P* value $<1 \times 10^{-5}$ were considered significant. Genes of interest were manually curated and highlighted.

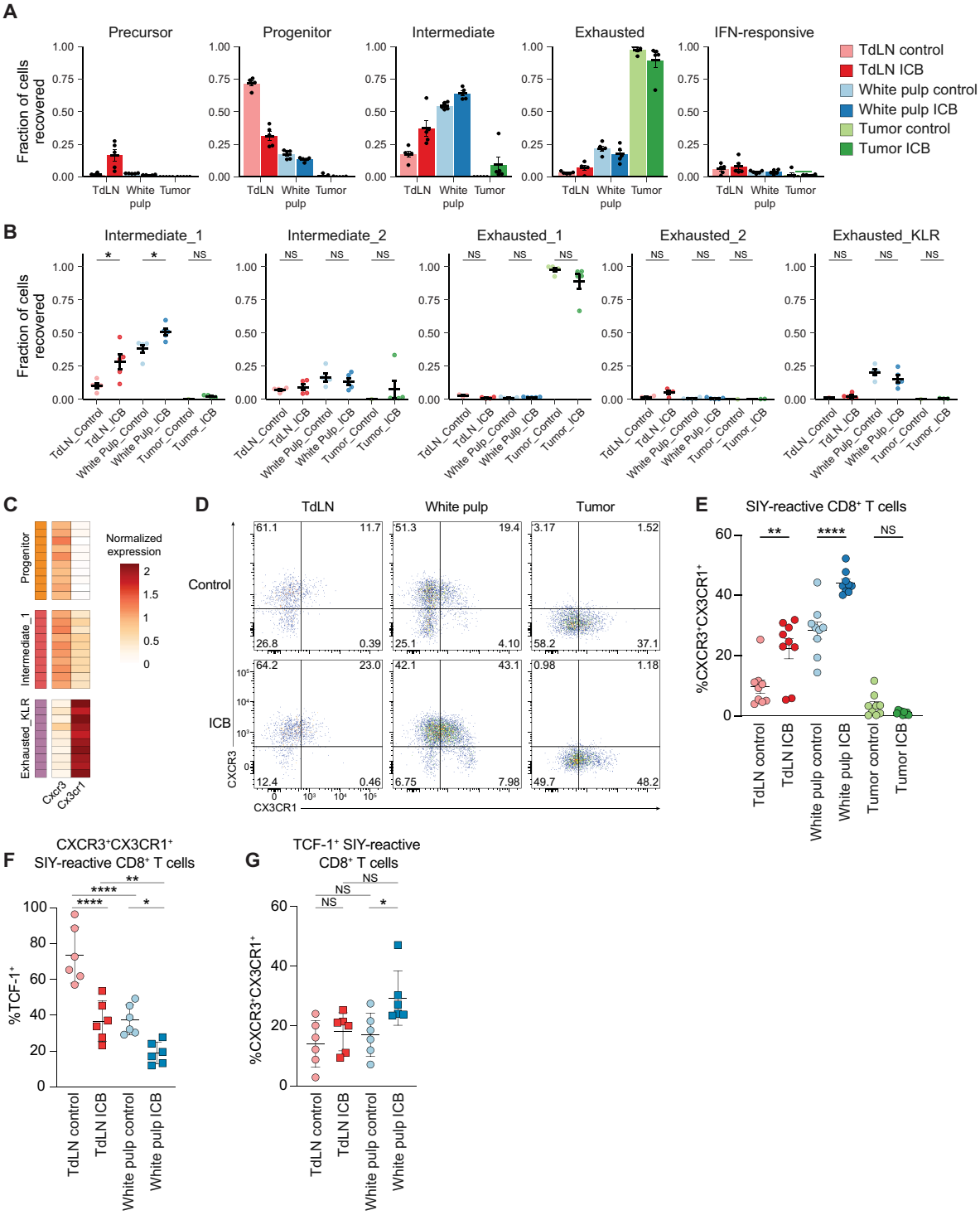

Fig. 3. Distribution of transcriptional states between TdLN, white pulp, and tumor. (**A**) Frequency of exhausted states in each tissue. (**B**) Frequency of transcriptional states associated with exhaustion in control and ICB-treated mice. *P* values were calculated using a two-sided Wilcoxon rank sum test and adjusted using Bonferroni correction. (**C**) Heatmap of normalized *Cxcr3* and *Cx3cr1* expression by progenitor, intermediate 1, and exhausted KLR T cells. Each box is the average expression in one mouse. (**D**) Representative flow cytometry plots of CXCR3 and CX3CR1 expression by SIY-reactive T cells in TdLN, white pulp (spleen), and tumor. (**E**) Quantification of $CXCR3^+CX3CR1^+$ SIY–reactive $CD8^+$ T cells in TdLN, white pulp (spleen), and tumor. (**F**) Frequency of TCF-1 expression by $CXCR3^+CX3CR1^+$ SIY–reactive $CD8^+$ T cells in the TdLN and spleen. (**G**) Frequency of $CXCR3^+CX3CR1^+$ cells among $TCF\text{-}1^+$ SIY–reactive $CD8^+$ T cells. For (E) to (G), $n = 6$, and *P* values were calculated with one-way ANOVA.

pretreatment and post-ICB conditions (Fig. 3E). These results were validated in MC38.SIY and LL/2.SIY tumor models (fig. S5C). Analysis of T cells in the white pulp or the blood-accessible red pulp revealed that the expansion of intermediate 1 CXCR3$^+$CX3CR1$^+$ T cells occurred predominantly within the white pulp (fig. S5, D to F). This was further supported by the result that the frequency of intermediate 1 T cells did not increase in the blood after ICB (fig. S5E). Together, these data identify the white pulp as a critical anatomical site for the expansion of intermediate 1 CD8$^+$ T cells upon ICB.

Several reports have demonstrated the importance of TCF-1 expression for CD8$^+$ T cells to respond to ICB (*2*, *19*, *22*–*24*, *27*). We examined the expression of TCF-1 among progenitor CXCR3$^+$CX3CR1$^-$, intermediate 1 CXCR3$^+$CX3CR1$^+$, and exhausted KLR CXCR3$^-$CX3CR1$^+$ T cell populations. Progenitor T cells expressed the highest levels of TCF-1 in both the TdLN and white pulp (fig. S6, A and B). In the white pulp, progressive differentiation into intermediate 1 and exhausted KLR T cells correlated with a gradual decrease in TCF-1 expression (fig. S6, A and B). Consistent with previous reports (*19*, *22*, *23*), the frequency of TCF-1$^+$ T cells among all three of these T cell subsets decreased in response to ICB, suggesting enhanced T cell differentiation in response to ICB (Fig. 3F and fig. S6, A and B). In addition, in both the TdLN and white pulp, progenitor T cells comprised most TCF-1$^+$ SIY–reactive T cells (fig. S6, C and D). The frequency of intermediate 1 T cells among TCF-1$^+$ SIY–reactive T cells remained unchanged in the TdLN after ICB (fig. S6, C and D). In contrast, in the white pulp, the fraction of intermediate 1 T cells among TCF-1$^+$–expressing SIY-reactive T cells increased after ICB, supporting that the expansion of this population constitutes a critical component of the T cell response elicited by ICB (Fig. 3G and fig. S6, C and D).

In addition, we assessed the expression of GZMB, PD-1, and TIM-3 across these T cell populations. Intermediate 1 CXCR3$^+$CX3CR1$^+$ T cells expressed the highest level of GZMB, suggesting that these cells exhibit enhanced cytotoxic capacity (fig. S7, A and B). In the TdLN, progenitor CXCR3$^+$CX3CR1$^-$ and intermediate 1 CXCR3$^+$CX3CR1$^+$ T cells displayed similar frequencies of TIM-3 and PD-1 expression (fig. S7, C to F). However, in the white pulp, the frequency of TIM-3 expression was highest among intermediate 1 CXCR3$^+$CX3CR1$^+$ T cells, whereas the frequency of PD-1 expression was reduced in exhausted KLR CXCR3$^-$CX3CR1$^+$ T cells (fig. S7, C to F). Together, these results indicate that the frequency of distinct transcriptional states associated with the progression of T cell exhaustion varies among the tumor, TdLN, and spleen. Moreover, treatment with ICB selectively expands CD8$^+$ T cells with an intermediate 1 phenotype that express elevated levels of effector molecules in both the white pulp and TdLN.

CXCR3$^+$CX3CR1$^+$ intermediate-exhausted T cells give rise to clonally distinct exhausted 1 or exhausted KLR T cell phenotypes

To gain insights into the relationships among the expanded T cell clusters, we next examined the TCR repertoire of SIY-reactive T cells (Fig. 4A). In untreated mice, we observed the largest levels of clonal expansion in the white pulp, whereas in mice treated with ICB, the magnitudes of clonal expansion observed were similar among the tumor, TdLN, and white pulp (Fig. 4B). Consistent with this observation, TCR repertoire diversity decreased after ICB treatment, indicating that ICB promotes strong expansion of a subset of tumor-reactive clonotypes (Fig. 4C). We also observed a greater clonal richness (i.e., total number of SIY-reactive clonotypes), demonstrating that ICB treatment simultaneously enables maintenance of a larger repertoire of tumor-reactive T cells (Fig. 4D).

We next sought to define a hierarchy underlying the path of differentiation of tumor-reactive clonotypes. We considered a clonotype representative of a phenotype if at least two T cells from that clonotype were found in any given phenotype. On the basis of this definition, we constructed a heatmap of the representative phenotypes present within individual TCR clonotypes (Fig. 4E). We then computed a transition matrix using the geometric mean overlap of clonotypes between each pair of phenotypes (Fig. 4F). We found that the repertoire of progenitor clonotypes shared substantial overlap with the repertoire of precursor clonotypes, consistent with precursor T cells undergoing differentiation to progenitor T cells. Likewise, intermediate 1 clonotypes exhibited the greatest clonal overlap with progenitor clonotypes, suggesting that intermediate 1 T cells differentiate from progenitor T cells. Both the exhausted 1 and exhausted KLR clonotypes demonstrated the greatest clonal overlap with intermediate 1 clonotypes, suggesting that most exhausted 1 and exhausted KLR T cells differentiate from intermediate 1 T cells. The level of clonal overlap between exhausted 1 and exhausted KLR phenotypes was minimal, suggesting that they represent distinct, noninterconvertible T cell states. Consistent with this analysis, upset plots depicting the patterns of phenotypic variation within clonotypes demonstrated that the most common pairs of phenotypes identified within a single clonotype were progenitor–intermediate 1, intermediate 1–exhausted 1, progenitor–intermediate 2, intermediate 1–exhausted KLR, and intermediate 1–intermediate 2 (fig. S8A). Thus, we developed a model in which precursor T cells differentiate into progenitor T cells that in turn give rise to intermediate 1 and intermediate 2 T cells. Intermediate 1 T cells can bifurcate to either exhausted 1 T cells or exhausted KLR T cells (Fig. 4G). This model demonstrates high levels of concordance with recent studies of chronic viral infection in mice (*32*, *33*), which include an intermediate phenotype preceding divergent exhausted phenotypes.

Tumor-specific T cell differentiation is associated with tissue-site trafficking

We next assessed the relationship between the differentiation of individual clonotypes and their tissue location. We found a robust correlation between the frequencies of individual clonotypes among the tumor, TdLN, and spleen, indicating that these tissues are populated by a common pool of SIY-reactive, tumor-specific clonotypes (Fig. 5A). Using the constructed heatmap (Fig. 4E), we identified the two most common phenotypes encountered within each clonotype, allowing us to classify clonotypes as either belonging to only a single phenotype or transitioning from one phenotype to another (Fig. 4E). Clonotypes in which we could not unambiguously assign to one or two dominant phenotypes were excluded from this analysis. Comparing the clonal sizes and phenotypes present at each tissue site within transitioning clonotypes, we found that clonotypes differentiating from the progenitor state to intermediate 1 were strongly polarized toward the progenitor phenotype in the TdLN but were polarized toward the intermediate 1 phenotype in the white pulp, suggesting that transition between these two transcriptional states is strongly associated with the migration of T cells from the TdLN to the spleen (Fig. 5B and fig. S8B). Likewise, the transition between the intermediate 1 and exhausted 1 phenotypes was strongly associated with trafficking from the white pulp to the tumor (Fig. 5C). In contrast, although a small

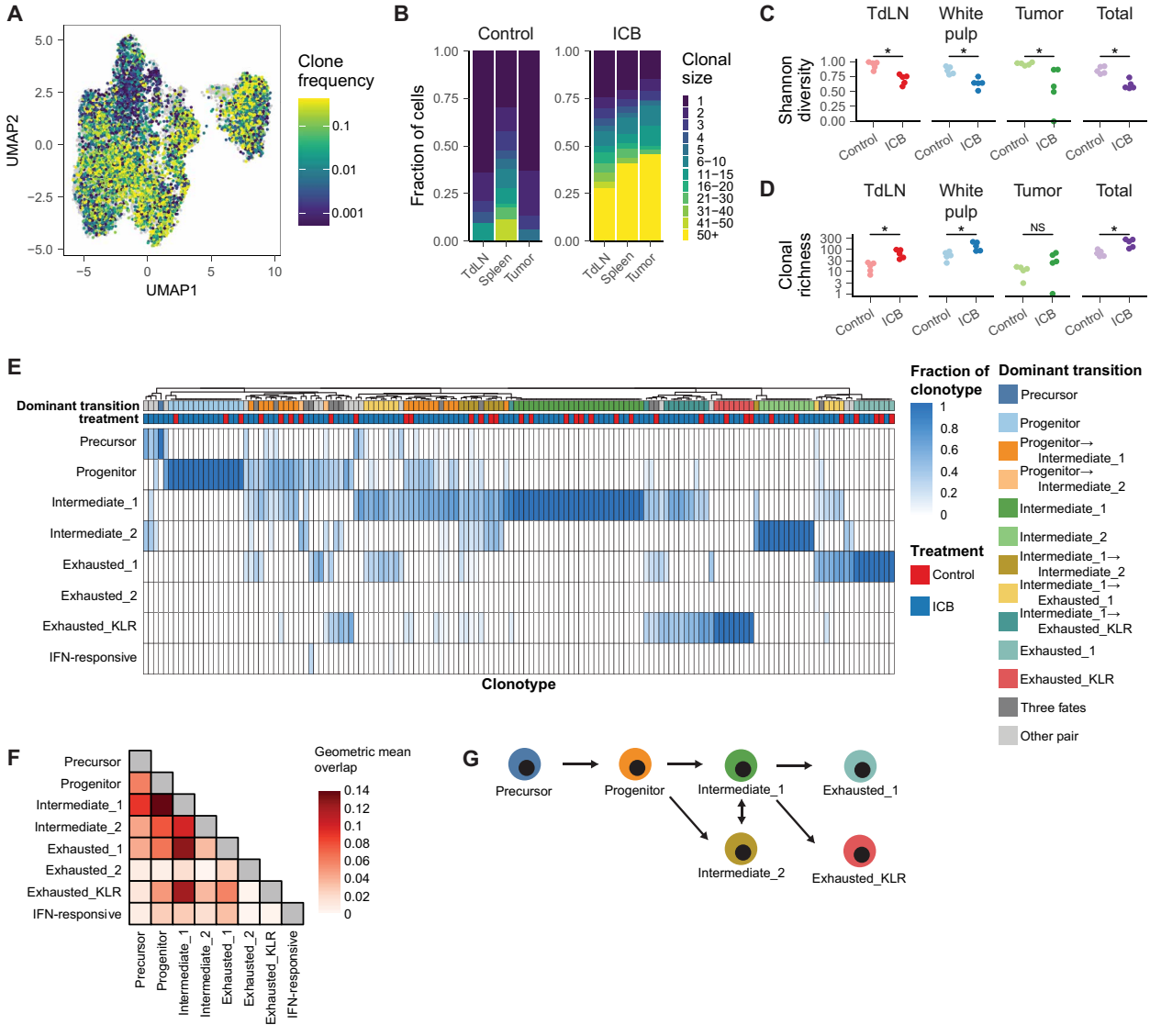

Fig. 4. Clonal dynamics of SIY-reactive CD8$^+$ T cells. (**A**) UMAP of SIY-reactive CD8$^+$ T cells colored by clonal size. (**B**) Stacked bar plots of clonal sizes among TdLNs, white pulp (spleen), and tumors of control and ICB-treated mice. Clonal sizes were computed separately in each tissue. (**C**) Shannon diversity of TCR repertoire. (**D**) Clonal richness of TCR repertoire. For (C) and (D), $n = 5$, and P values were calculated using a two-sided Wilcoxon rank sum test and adjusted using Bonferroni correction. (**E**) Heatmap of phenotypes present within individual TCR clonotypes. A random sample of the top 150 most expanded clones is shown. Phenotypes present only once within a single clonotype are not shown. (**F**) Transition matrix of transcriptional states. Boxes are shaded according to the geometric mean of normalized clonal frequencies between pairs of transcriptional states. (**G**) Proposed model of T cell differentiation informed by clonal trajectories.

number of cells from clonotypes undergoing differentiation from intermediate 1 to exhausted KLR states demonstrated an intermediate 1 phenotype in the TdLN, most of these clonotypes were absent from both the TdLN and the tumor but present in the white pulp, indicating that these transitions primarily occur within the spleen (Fig. 5D and fig. S8C). Overall, these results demonstrate that clonally related T cells have distinct phenotypes in different tissues and that select phenotypic transitions, including progenitor to intermediate 1 and intermediate 1 to exhausted 1, are strongly associated with trafficking from one tissue to another, whereas others, such as intermediate 1 to exhausted KLR, are not accompanied with a change in tissue site and instead take place primarily among cells resident in the spleen.

The intermediate 1–to–exhausted 1 transition limits clonal differentiation and is overcome by ICB

To determine how ICB modulates the phenotypic transitions experienced by SIY-reactive clonotypes, we examined the distribution of clonal behaviors present in control and ICB-treated mice. Although the frequency of clonotypes classified as transitioning between intermediate 1 and exhausted 1 was similar (fig. S8D), the fraction of T cells belonging to an intermediate 1 ➔ exhausted 1–transitioning clonotype was substantially greater in mice treated with ICB (Fig. 5E). We then calculated the absolute clonal sizes of individual clonotypes in control and ICB-treated mice undergoing the clonal transitions analyzed above. We also found that the clonal sizes of intermediate 1 ➔ exhausted 1 clonotypes, but no other transitioning

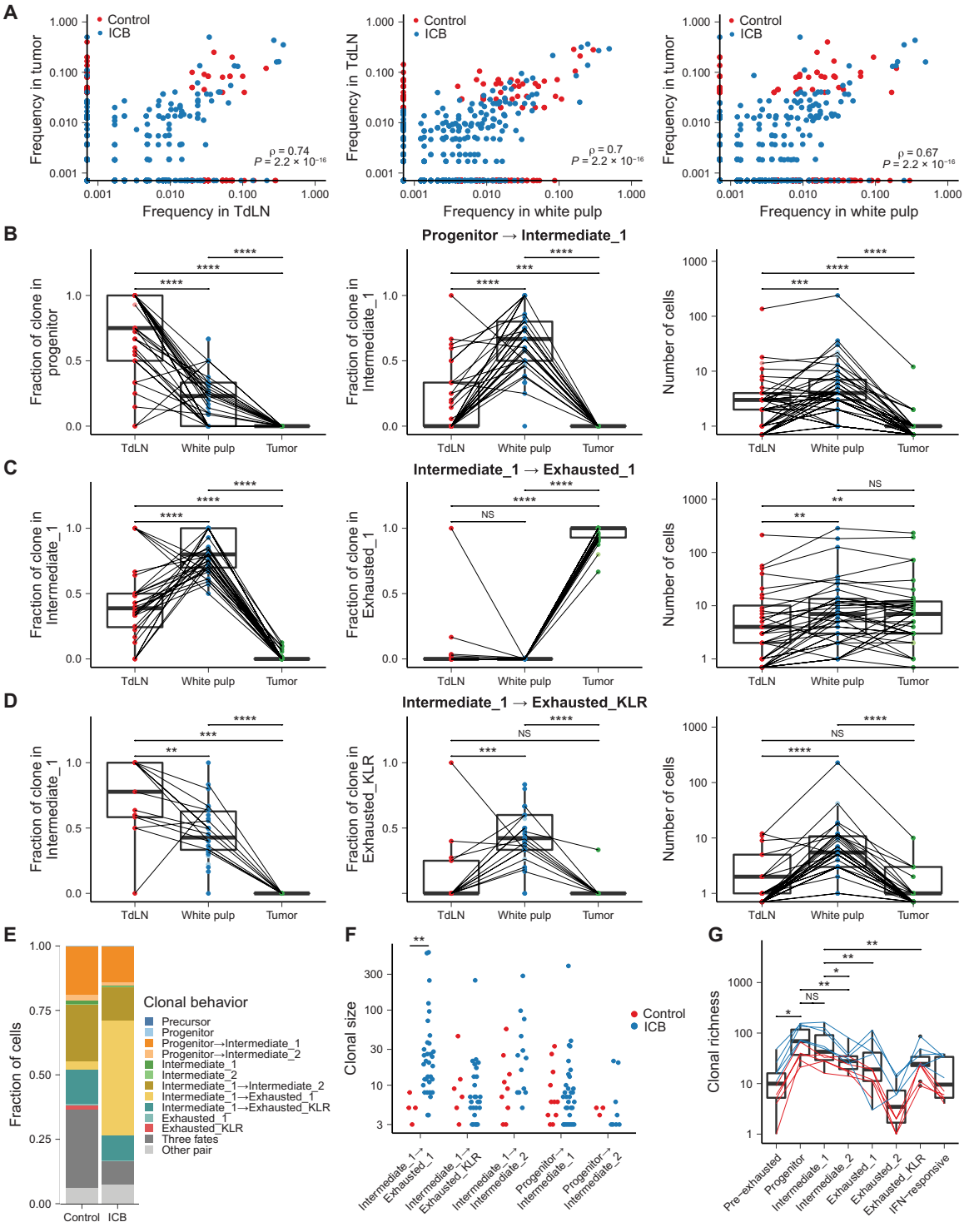

Fig. 5. Clonal differentiation is accompanied by change in anatomic site. (**A**) Correlation between clonotype frequencies in the tumor, TdLN, and white pulp (spleen). (**B**) Tissue-site distribution of progenitor and intermediate 1 phenotypes and clonal sizes in progenitor→intermediate 1 clones. (**C**) Tissue-site distribution of intermediate 1 and exhausted 1 phenotypes and clonal sizes in intermediate 1 → exhausted 1 clones. (**D**) Tissue-site distribution of intermediate 1 and exhausted KLR phenotypes and clonal sizes in intermediate 1 → exhausted KLR clones. For (A) to (D), *P* values were calculated with a paired, two-sided Wilcoxon rank sum test and adjusted with Bonferroni correction. Boxes show interquartile range (IQR) with 1.5× IQR whiskers. (**E**) Stacked bar chart of clonal behaviors assigned to single cells in control and ICB-treated mice. Only clonotypes consisting of more than two cells are shown. (**F**) Absolute clonal sizes of transitioning clonotypes in control and ICB-treated mice. *P* values were calculated with a two-sided Wilcoxon rank sum test and were adjusted with Bonferroni correction. (**G**) Clonal richness of transcriptional phenotypes in control and ICB-treated mice. *P* values were calculated with a paired, two-sided Wilcoxon rank sum test and adjusted with Bonferroni correction. Boxes show IQR with 1.5× IQR whiskers.

clonotypes, were significantly larger in mice treated with ICB, suggesting that ICB preferentially expands intermediate 1 clonotypes that are primed to undergo an intermediate 1–to–exhausted 1 transition (Fig. 5F).

We also computed the clonal richness of each phenotype encountered on our hypothesized differentiation trajectory (Fig. 5G). We found that clonal richness peaked at the progenitor and intermediate 1 phenotype, suggesting that precursor T cells, the apparent direct precursors of progenitor T cells, are largely depleted by day 14 after tumor inoculation. In addition, this result demonstrates that there is an accumulation of clonotypes at the progenitor and intermediate 1 phenotype. These data suggest that although the transition from progenitor to intermediate 1 phenotype is efficient, occurring with high probability, the transition from intermediate 1 to an exhausted 1 phenotype is inefficient and that the intermediate 1 phenotype is a rate-limiting step encountered during clonal differentiation. Thus, we concluded that one of the major results of ICB treatment is the expansion of splenic intermediate 1 clonotypes that are predisposed to undergo the intermediate 1–to–exhausted 1 transition.

Splenic intermediate 1 T cells drive the expansion of tumor-reactive CD8$^+$ T cells during ICB

To confirm that the ability of tumor-reactive CD8$^+$ T cells to expand in response to ICB was different between T cells from the TdLN and white pulp, we performed an adoptive transfer of TCR-transgenic in vivo–activated 2C T cells into KP.SIY tumor–bearing mice (Fig. 6A). In this system, expanded 2C T cells appear with comparable frequency and number in both the TdLNs and white pulp of mice within 72 hours after transfer (Fig. 6, B and C, and fig. S9, A and B) and transcriptionally mirror endogenous SIY-reactive T cells (*8*, *9*). CellTrace violet dilution studies of labeled 2C T cells 72 hours after transfer showed that 2C T cells undergo four to six cell divisions in the TdLN, whereas they undergo eight or more divisions in the white pulp (Fig. 6, D and E), confirming that priming takes place in the TdLN, followed by splenic trafficking.

We next investigated the phenotypes of transferred 2C T cells in TdLNs and white pulp of recipient mice. Consistent with our previous data, more 2C T cells in the white pulp displayed an intermediate 1 CXCR3$^+$CX3CR1$^+$ phenotype compared with 2C T cells in the TdLN (Fig. 6, F and G, and fig. S9C). This observation supports that differentiation from a progenitor to intermediate 1 T cell state is associated with trafficking to the spleen. Further, progenitor CXCR3$^+$CX3CR1$^-$ and intermediate 1 CXCR3$^+$CX3CR1$^+$ T cells in the white pulp expressed similar levels of PD-1, whereas intermediate 1 T cells exhibited reduced SLAMF6 expression, a proxy for TCF-1 (*19*), aligning with our prior findings on endogenous SIY-reactive CD8$^+$ T cells (figs. S9, D and E, S6B, and S7F). Overall, these data support a model in which transferred 2C T cells initially proliferate in the TdLN before trafficking to the white pulp of the spleen, where they undergo additional cycles of proliferation and acquire a more differentiated CXCR3$^+$CX3CR1$^+$ intermediate 1 T cell phenotype.

We next used a serial adoptive transfer approach to determine whether splenic 2C T cells exhibited enhanced responsiveness to ICB. We sorted 2C T cells from TdLNs and white pulp of primary recipient mice and transferred the sorted 2C T cells to secondary recipients with time-matched KP.SIY tumors (Fig. 6H). Only 2C T cells sorted from the white pulp of mice significantly expanded in response to ICB (Fig. 6I and fig. S10, A and B). Further, GZMB expression by 2C T cells in the tumor was up-regulated after ICB treatment (fig. S10C). These data indicate that splenic T cells, which are enriched for the intermediate 1 phenotype, are the primary responders to ICB and can recirculate to both TdLNs and tumors.

Antigen density regulates intermediate 1 T cell differentiation and trafficking

We sought to further understand the regulators of tumor-reactive CD8$^+$ T cell differentiation in the spleen. Chronic antigen stimulation is known to drive T cells into terminal exhaustion states (*12*, *13*). Consistently, SIY-reactive CD8$^+$ T cells infiltrating the tumor almost completely comprised an exhausted 1 phenotype. Progenitor-exhausted CD8$^+$ T cells are also induced by high antigen levels in the lymph node (*17*), but how antigen affects differentiation of T cells into the intermediate 1 phenotype is unknown. To examine the extent of antigen trafficking to the spleen, we inoculated mice with KP cells that expressed the pH-stable fluorophore ZsGreen (KP.ZsGreen) and examined the levels of ZsGreen in CD45$^+$ cells in TdLNs and spleens. TdLNs had a significantly higher frequency of ZsGreen$^+$CD45$^+$ cells compared with spleens, indicating that the spleen was a relatively antigen-low anatomic site (fig. S11, A and B). Using the 2C T cell adoptive transfer approach, we then determined whether antigen was required to drive tumor-reactive CD8$^+$ T cell expansion in the spleen. We primed 2C T cells in vivo in primary KP.SIY tumor–bearing host mice before transferring 2C T cells isolated from the white pulp into secondary hosts bearing either KP.SIY or KP tumors. Secondary hosts were treated with ICB (Fig. 7A). 2C T cells failed to accumulate in secondary hosts bearing KP tumors, indicating that antigen was required, even at low levels, for 2C T cell expansion in response to ICB (Fig. 7B and fig. S11, C and D).

On the basis of these results, we aimed to determine whether T cell expansion in the spleen is dependent on DC-mediated antigen presentation. Previous work has shown that cross-presenting DCs (DC1s), driven by the transcription factor Batf3, are the dominant DC subset that prime CD8$^+$ T cells in TdLNs (*8*, *37*). Further, we observed that splenic DC1s are exclusively present in the white pulp (fig. S12, A to C). Thus, we compared the expansion of adoptively transferred 2C T cells in Batf3$^{-/-}$ hosts with wild-type hosts after ICB therapy (Fig. 7C). Consistent with prior studies, we observed poor infiltration into the tumor and a reduced expansion of 2C T cells in the TdLNs of Batf3$^{-/-}$ hosts (Fig. 7D and fig. S12, D and E) (*38*–*40*). We also observed a fivefold reduction in the expansion of SIY-reactive T cells in the spleens of Batf3$^{-/-}$ mice (Fig. 7D and fig. S12, D and E). Further, Batf3$^{-/-}$ mice had a reduction in the proportion of 2C T cells with an intermediate 1 CXCR3$^+$CX3CR1$^+$ phenotype in the white pulp, whereas the less differentiated progenitor CXCR3$^+$CX3CR1$^-$ T cell state was enriched (fig. S12, F and G).

Next, we aimed to specifically address whether levels of systemic antigen affect the expansion of antigen-reactive intermediate 1 T cells in the spleen. To directly test this, we isolated splenocytes from naïve mice, pulsed them with SIY, and transferred them into KP.SIY tumor–bearing mice, which were subsequently treated with ICB (Fig. 7E). This approach systemically increases cell-associated antigen and enhances cross-presentation, including in the spleen (*41*, *42*). On day 14 after tumor inoculation, we observed accelerated differentiation of tumor-reactive T cells, as evidenced by the decrease in progenitor CXCR3$^+$CX3CR1$^-$ T cells in the white pulp, and to a lesser degree in the TdLNs, of mice that received SIY-pulsed

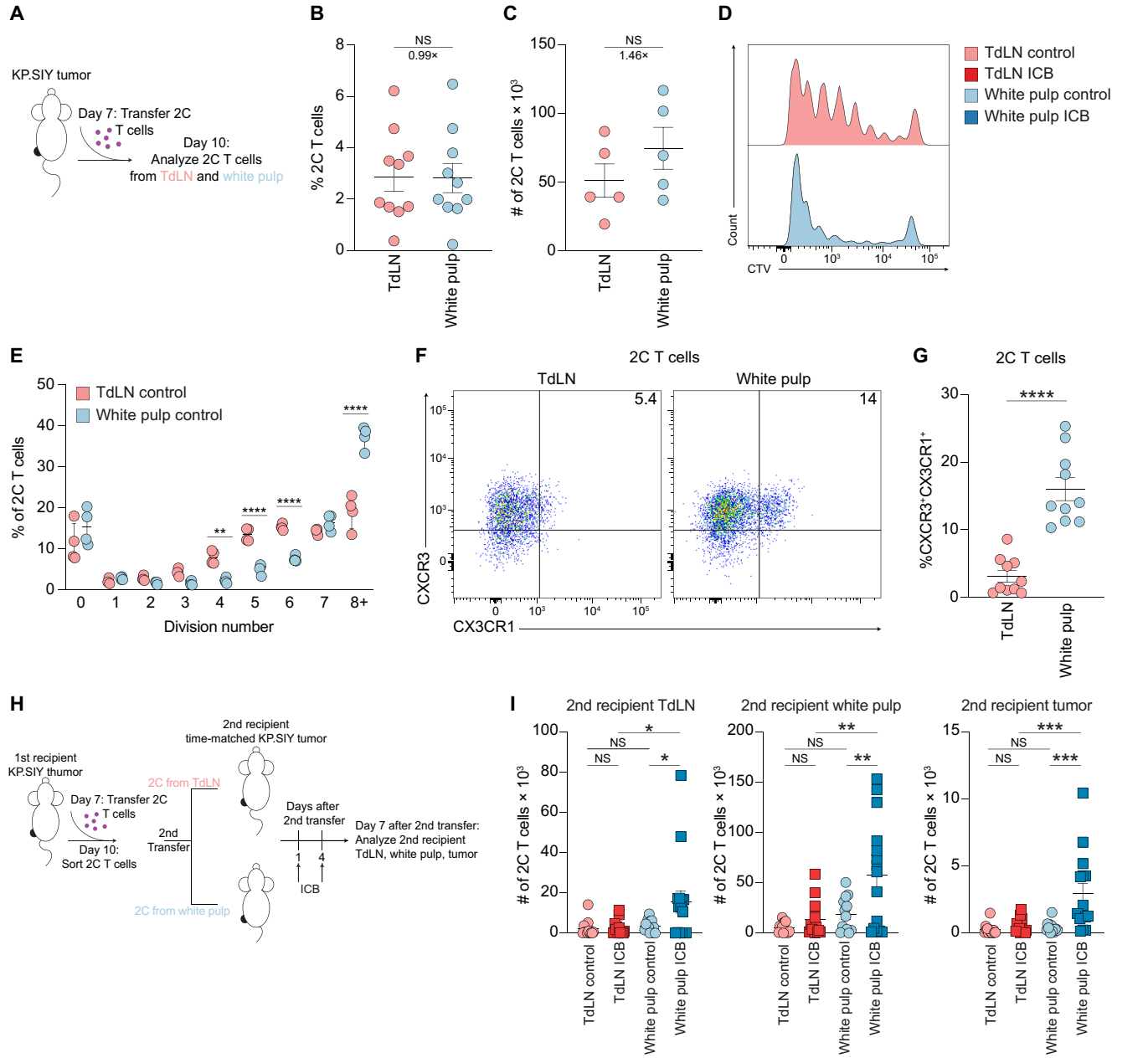

Fig. 6. Splenic tumor-reactive CD8$^+$ T cells drive the response to ICB. (**A**) Adoptive transfer experimental design. (**B** and **C**) Frequency (B) and number (C) of 2C T cells in the TdLN and spleen 3 days after transfer into KP.SIY flank tumor–bearing mice, $n = 10$ (B) and $n = 5$ (C). *P* values were calculated with a Mann-Whitney *U* test. (**D**) CTV dilution of 2C T cells in the TdLN and white pulp (spleen) 3 days after transfer into KP.SIY flank tumor–bearing mice. (**E**) Quantification of the fraction of 2C T cells in each cell division; $n = 4$; *P* values calculated with one-way ANOVA. (**F**) Phenotype of 2C T cells 3 days after transfer to KP.SIY flank tumor–bearing mice. (**G**) Quantification of the phenotype of 2C T cells 3 days after transfer to KP.SIY flank tumor–bearing mice, $n = 10$. *P* values were calculated with a Mann-Whitney *U* test. (**H**) Experimental design of 2C T cell transfer into secondary recipients. (**I**) Accumulation of transferred 2C T cells in secondary recipients. TdLN control $n = 13$, TdLN ICB $n = 13$, spleen control $n = 14$, and spleen ICB $n = 15$. *P* values calculated with one-way ANOVA.

splenocytes (fig. S12, H and I). Elevated levels of systemic antigen increased the proportion of intermediate 1 CXCR3$^+$CX3CR1$^+$ T cells in untreated mice but not in ICB-treated animals and abrogated the previously observed expansion of intermediate 1 T cells in mice that received ICB (Fig. 7, F and G). In addition and independently of ICB therapy, systemic antigen resulted in an increased frequency of exhausted KLR CXCR3$^-$CX3CR1$^+$ T cells in the white pulp (Fig. 7, F to H) accompanied by lower expression of CXCR3 and higher expression of CX3CR1 on intermediate 1 T cells (Fig. 7, I and J). Together, these results suggest that intermediate 1 T cells in the white pulp undergo accelerated differentiation to the exhausted KLR phenotype in response to increased levels of systemic antigen. This biased T cell differentiation toward exhausted KLR T cells in the white pulp in response to SIY-pulsed splenocytes was associated

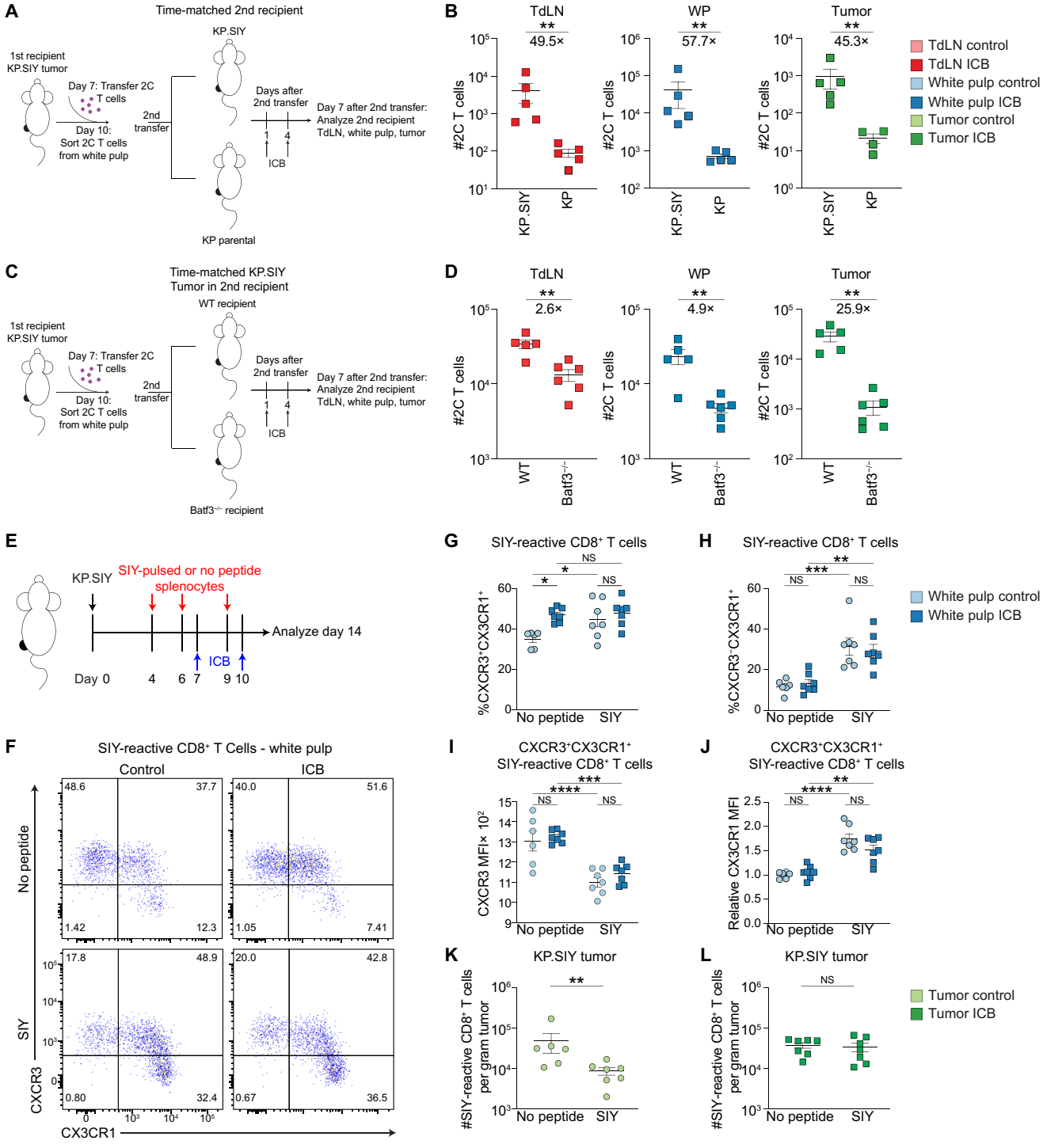

Fig. 7. Antigen levels and cross-presentation by DC1 affect SIY-reactive T cell differentiation in the spleen and subsequent trafficking to the tumor. (**A**) Experimental scheme of 2C T cell adoptive transfer into KP.SIY or KP flank tumor–bearing secondary recipients. (**B**) Numbers of recovered 2C T cells in secondary recipients with either KP.SIY or KP flank tumors, $n = 5$ (or 4 for KP tumors). *P* values were calculated with a Mann-Whitney *U* test. (**C**) Experimental scheme of 2C T cell adoptive transfer into KP.SIY flank tumor–bearing WT or Batf3$^{-/-}$ secondary recipients. (**D**) Numbers of recovered 2C T cells in KP.SIY flank tumor–bearing WT or Batf3$^{-/-}$ secondary recipients, $n = 5$. *P* values were calculated with a Mann-Whitney *U* test. (**E**) Experimental scheme of SIY-pulsed splenocyte transfer. (**F**) Example flow cytometry plots of SIY-reactive T cell expression of CXCR3 and CX3CR1 in the spleen. (**G**) Percentage of splenic SIY-reactive CD8$^+$ T cells that are CXCR3$^+$CX3CR1$^+$. (**H**) Percentage of splenic SIY-reactive CD8$^+$ T cells that are CXCR3$^-$CX3CR1$^+$. (**I**) CXCR3 mean fluorescence intensity (MFI) of splenic SIY-reactive CXCR3$^+$CX3CR1$^+$ CD8$^+$ T cells. (**J**) Relative CX3CR1 MFI of splenic SIY-reactive CXCR3$^+$CX3CR1$^+$ CD8$^+$ T cell population. (**K**) Number of SIY-reactive CD8$^+$ T cells per gram of KP.SIY tumor in control mice with or without SIY-pulsed splenocyte transfer. (**L**) Number of SIY-reactive CD8$^+$ T cells per gram of KP.SIY tumor in ICB-treated mice with or without SIY-pulsed splenocyte transfer. For (G) to (L), $n = 6$, and *P* values were calculated with one-way ANOVA [(G) to (J)] and a Mann-Whitney *U* test [(K) and (L)].

with a significant reduction in tumor-infiltrating SIY-reactive CD8$^+$ T cells in untreated mice but not in mice treated with ICB therapy (Fig. 7, K and L). Increasing systemic antigen did not influence the viability of tumor-infiltrating SIY-reactive CD8$^+$ T cells (fig. S12, J and K). This is consistent with our previous observation that exhausted KLR T cells reside primarily in the spleen and do not traffic to tumors (Fig. 3B). The observation that ICB therapy was able to rescue T cell infiltration into the tumor suggests that the remaining fraction of intermediate 1 T cells in SIY-pulsed mice can differentiate into sufficient numbers of tumor-trafficking, exhausted 1 T cells upon ICB, resulting in some degree of tumor control (fig. S12L). In sum, these results suggest that low but detectable levels of cross-presented antigen in the white pulp are critical for the accumulation and retention of splenic T cells in the intermediate 1 state and that perturbation of splenic intermediate 1 T cells can affect migration of T cells to the tumor.

Exhausted KLR T cells in human patients exhibit reduced migration to tumors relative to other tumor-homing clonotypes

To assess the extent to which the transcriptional phenotypes and clonotypic trends observed among SIY-reactive T cells in our mouse model are present in human patients, we conducted a reanalysis of a pan-cancer atlas of tumor-infiltrating lymphocytes recovered from 316 patients with cancer (*43*). We focused this analysis on a subset of the larger atlas, comprising four types of solid tumors (colorectal carcinoma, hepatocellular carcinoma, non–small cell lung cancer, and cholangiocarcinoma) for which scRNA and TCR sequencing data from matched tumor tissue and peripheral blood were available. On the basis of transcriptional expression, the authors annotated most CD8$^+$ T cells as naïve (Tn), memory (Tm), resident memory (Trm), effector memory (Tem), exhausted (Tex), terminally differentiated memory or effector cells (Temra), natural killer (NK)–like (Tk), or interferon-stimulated gene (ISG)–positive.

We first examined the concordance between SIY-reactive transcriptional phenotypes identified in our mouse model and the transcriptional phenotypes present among tumor-infiltrating lymphocytes from human patients. We found strong agreement between the signatures identified in our mouse model and the phenotypes annotated by Zheng *et al.*: Specifically, Tn expressed strong levels of our progenitor signature; Tm, Trm, and Tem up-regulated our intermediate 1 signature, with a subset of Trm also up-regulating our intermediate 2 signature; Tex up-regulated our exhausted 1 and exhausted 2 signatures; and Temra up-regulated our exhausted KLR signature (Fig. 8, A and C, and fig. S13). Thus, the transcriptional states present in our mouse model can differentiate phenotypes of T cells present in the tumors and peripheral blood of human patients, with Temra being the analogous counterpart of the exhausted KLR cells. Next, we analyzed T cells in the peripheral blood that were clonally related to tumor-infiltrating clonotypes. Temra cells in the peripheral blood were the only population increased in frequency among tumor-trafficking clonotypes relative to non–tumor-trafficking clonotypes, suggesting that this population in peripheral blood is enriched for tumor-specific CD8$^+$ T cells (Fig. 8D). The tumor-infiltrating clonal relatives of Temra cells from the peripheral blood were also enriched for a Temra phenotype relative to other tumor-infiltrating clonotypes found in peripheral blood, suggesting that this phenotype is conserved upon entry into the tumor (Fig. 8E).

To determine whether trafficking of T cells into the tumor was associated with any specific T cell state, we assessed the fraction of T cells within each state between tumor and peripheral tissues. Strikingly, among tumor-trafficking clonotypes, the Temra phenotype was substantially decreased in frequency in the tumor relative to peripheral blood, suggesting poor tumor infiltration (Fig. 8F). In contrast, Trm, Tem, and ISG cells exhibited an increase in frequency in the tumor, suggesting that these populations undergo efficient recruitment to the tumor. To assess whether these trends in tumor trafficking potential were apparent at the level of individual clonotypes, we computed the ratio between the frequency of each clonotype in the tumor and the blood. Relative to other clonotypes in the peripheral blood, Temra clonotypes were substantially more expanded in peripheral blood compared with the tumor, indicating that individual Temra clonotypes exhibit a reduced ability to enter the tumor relative to other phenotypes in the peripheral blood (Fig. 8G). Considering this observation in human tumors, we revisited our analysis of exhausted KLR T cells in the blood and observed an increase in frequency of exhausted KLR T cells in the blood of both control and ICB-treated mice, with only a modest expansion in the white and red pulp of the spleen after ICB (Fig. 8H). These data are consistent with the finding that the human analog of the exhausted KLR T cell population resides primarily in the blood but not cancerous tissue (Fig. 8H). Overall, these data support our model in which intermediate 1–like T cells (Tm, Trm, and Tem) undergo efficient entry into the tumor from lymphoid tissues, whereas exhausted KLR-like clonotypes (Temra) exhibit a decreased potential to migrate to the tumor, especially considering their relative level of clonal expansion within peripheral blood.

DISCUSSION

Here, we analyzed tumor-reactive CD8$^+$ T cells from tumors, TdLNs, and white pulp of ICB-treated and untreated mice with scRNA-seq and TCR sequencing. Our findings corroborate previous reports on the step-wise differentiation along distinct transcriptional phenotypes (*32*, *33*) and demonstrate that these transcriptional states appear largely restricted to individual anatomic sites. We observed that the intermediate 1 T cell population is enriched in the white pulp of the spleen and gives rise to two terminally differentiated populations of CD8$^+$ T cells: exhausted 1, which is largely restricted to the tumor, and exhausted KLR, which is enriched in the blood of mice and humans. Whereas increasing systemic antigen promoted the differentiation of intermediate 1 to the exhausted KLR T cell state, the absence of antigen or cross-presenting DCs reduced differentiation of intermediate 1 T cells in the white pulp, suggesting that some level of antigen on DCs is necessary to sustain T cells in the intermediate 1 phenotype. Together, our results demonstrate that microenvironmental factors present in individual anatomic sites play a role in guiding exhausted T cell differentiation and are critical in determining the outcome of ICB.

The spleen is frequently analyzed in models of chronic viral infection including LCMV, but in these models, the spleen is also a primary site of infection. In contrast, the spleen is rarely studied in the context of cancer (*19*, *22*–*24*, *26*, *27*). We found that splenic intermediate 1 T cells exhibit the greatest expansion in response to ICB. Consistent with this result, a recent study proposed that intermediate-exhausted T cells are most expanded by anti–PD-L1 treatment in murine LCMV infection (*32*). We found that a subset of intermediate 1 T cells retains

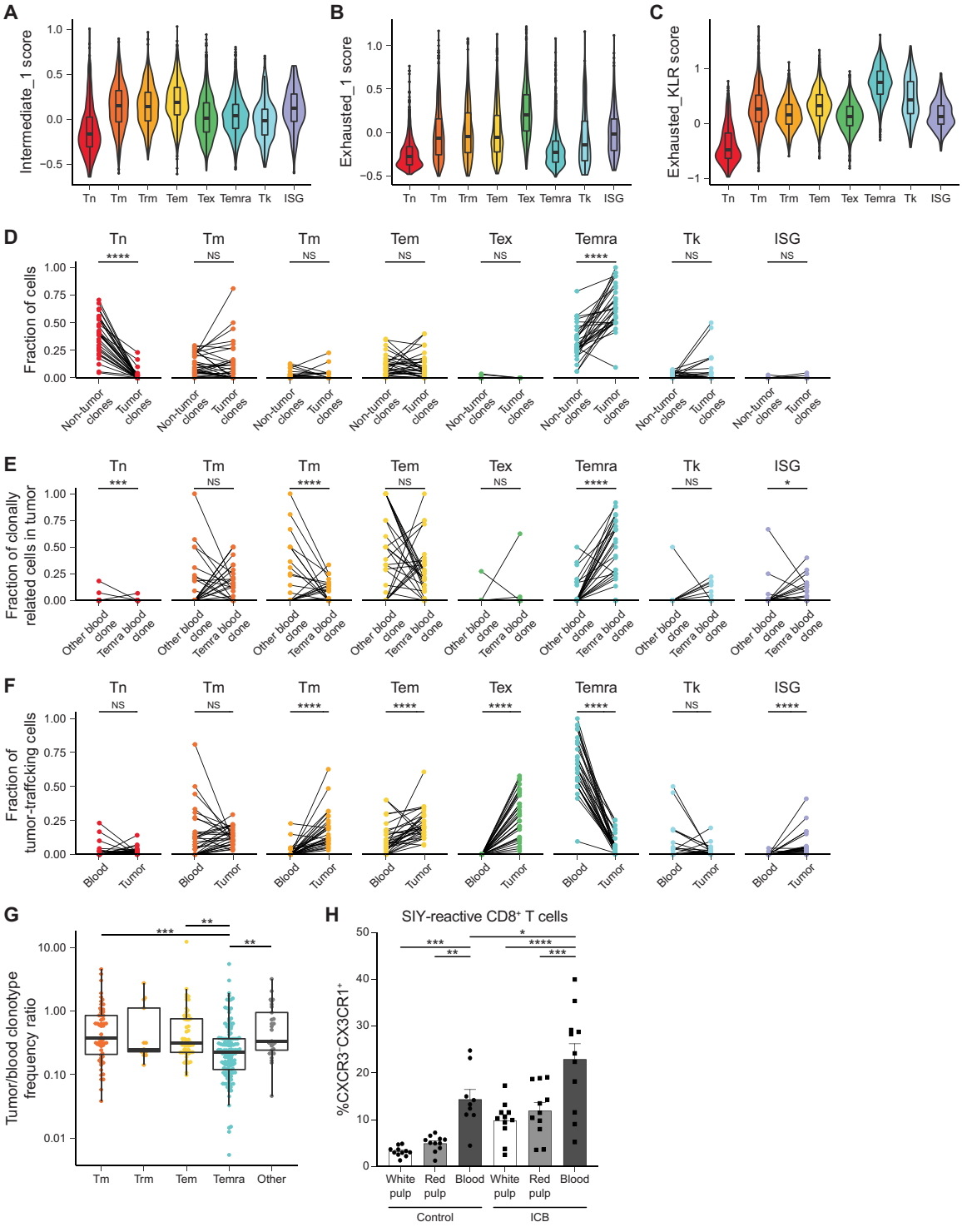

Fig. 8. Exhausted KLR cells in human patients exhibit decreased migration from peripheral blood to tumor. (**A** to **C**) Expression of signatures for intermediate 1, exhausted 1, and exhausted KLR phenotypes on clusters defined by Zheng *et al.* (*43*). Boxes show IQR with 1.5× IQR whiskers. (**D**) Frequency of phenotypes present in peripheral blood among tumor-trafficking and non–tumor-trafficking clonotypes. *P* values were calculated with a two-sided Wilcoxon rank sum test and adjusted with Bonferroni correction. (**E**) Frequency of phenotypes present among tumor-infiltrating T cells related to Temra clonotypes from peripheral blood and all other tumor-infiltrating clonotypes. *P* values were calculated with a two-sided Wilcoxon rank sum test and adjusted with Bonferroni correction. (**F**) Frequency of phenotypes present among tumor-trafficking $CD8^+$ T cells in blood and tumor. *P* values were calculated with a two-sided Wilcoxon rank sum test and adjusted with Bonferroni correction. (**G**) Ratio of clonal frequency in tissue to clonal frequency among Tm, Trm, Tem, Temra, and all other clonotypes. *P* values were calculated by a Kruskal-Wallis rank sum test followed by Dunn's posttest. Boxes show IQR with 1.5× IQR whiskers. (**H**) Frequency of endogenous $CXCR3^-CX3CR1^+$ exhausted KLR SIY-reactive $CD8^+$ T cells from the white pulp, red pulp, and blood of day 14 KP.SIY tumor–bearing mice; $n = 11$; *P* values calculated with one-way ANOVA.

TCF-1 expression, consistent with previous reports identifying TCF-1$^+$ CD8$^+$ T cells as the mediators of T cell self-renewal and expansion in response to ICB (*2*, *19*, *22*–*24*, *27*). Moreover, the proportion of intermediate 1 T cells within the TCF-1$^+$ splenic SIY-reactive T cell population strongly increased after ICB, reinforcing the idea that the expansion of this subset plays a crucial role in the T cell response induced by ICB.

Intermediate 1 T cells also bear some resemblance to a population of "transitory" proliferating cells reported to express CX3CR1 (*22*, *44*). These studies have suggested that these transitory T cells are derived directly from CXCR5$^+$ progenitor T cells; our data suggest that most ICB-triggered expansion can be attributed to cells undergoing transitions from intermediate 1 to exhausted 1. A reported population of CXCR5$^+$ CD8$^+$ progenitor exhausted T cells, which proliferated after PD-L1 blockade, also express CXCR3 and bear strong similarities to intermediate 1 T cells (*23*). It may be that in cancer, the intermediate 1 population combines aspects of progenitor and transitory T cells found in chronic LCMV infection. Intermediate 1 T cells therefore likely have a greater role in the response to ICB than previously appreciated, especially in cancer. We propose that these patterns of tissue-restricted antigen presence may encourage important yet transient antigen encounter in infected or tumor tissue and their draining lymph nodes, followed by low-density antigen encounter in the spleen. Our work highlights the crucial role of cross-presentation by DC1s in facilitating optimal T cell differentiation, even in scenarios of low antigen density. This pattern of antigen encounter may represent a key component of the antitumor immune response that is not well-modeled by chronic LCMV infection, which results in high antigen levels in the spleen.

Similar to previous studies (*32*, *33*), we found that the intermediate 1 population served as a hub for differentiation into multiple phenotypic states, including exhausted 1 and exhausted KLR T cells. Of these phenotypes, only exhausted 1 cells exhibited efficient trafficking to the tumor, suggesting that state decisions made at this bottleneck substantially affect the effectiveness of an antitumor T cell response. These two T cell states also exhibited minimal clonal overlap, suggesting that they represent divergent fates and raising the possibility that TCR signaling characteristics may influence fate decisions. Prior studies have demonstrated that higher TCR affinity promotes differentiation into a terminally exhausted phenotype rather than a phenotype resembling exhausted KLR (*33*). Future studies could seek to understand factors that regulate the fate commitment of intermediate 1 T cells and assess to what extent these transitions may be reversible. Understanding how to effectively target and manipulate the intermediate 1 to exhausted 1 fate decision may offer new strategies to increase the tumor-infiltrating abilities of T cells and enhance the efficacy of ICB.

By examining the relationships between anatomic sites and transcriptional phenotypes within individual clonotypes, we observed that some phenotypic transitions, including progenitor ➔ intermediate 1 and intermediate 1 ➔ exhausted 1, are strongly associated with transit between different tissues. We are unable to conclude whether entry into different tissues is a key factor promoting differentiation or whether differentiation itself promotes transit to different tissue sites. One previous study found, however, that full effector differentiation of progenitor T cells requires entry into the tumor, suggesting that T cell state transitions can result from trafficking to new anatomic locations (*45*).

In contrast with intermediate 1 T cells, our results indicate that mouse and human CX3CR1^{hi} CD8$^+$ T cells, including exhausted KLR and Temra T cells, respectively, do not traffic efficiently to the tumor. This result is consistent with previous findings where CX3CR1^{hi} memory CD8$^+$ T cells were preferentially found in blood, whereas CXCR3$^+$CX3CR1^{int} memory T cells, which phenotypically resemble intermediate 1 T cells, were resident in nonlymphoid tissues (*46*). These differential homing patterns may be explained by the expression of CXCR3. Intermediate 1 T cells express significantly more CXCR3 than exhausted KLR cells, and CXCR3 expression is critical for the homing of CD8$^+$ T cells into tumors (*47*). Consistent with our finding of inefficient tumor homing by exhausted KLR T cells, two previous studies using subcutaneous mouse models of cancer found that CX3CR1^{hi} CD8$^+$ T cells contribute little to antitumor immunity (*48*, *49*). One could imagine, however, that a population of circulating or spleen-patrolling tumor-reactive CD8$^+$ T cells could surveil for disseminated tumor cells and protect against metastasis (*50*). Thus, future studies could focus on the contributions of exhausted KLR CD8$^+$ T cells to antitumor immunity, including whether these cells can eventually reach the tumor and undergo differentiation to a tumor-homing exhausted 1 phenotype. These populations could also potentially provide a blood-based biomarker for antitumor immunity or response to ICB (*51*).

One limitation of our study is that there remain insufficient available data from tumor-reactive CD8$^+$ T cells recovered from the TdLNs and spleens of human patients with cancer to assess to what extent the transcriptional states and phenotypic transitions that we identified in our mouse models reflect patterns of differentiation experienced by antitumor CD8$^+$ T cells in human patients with cancer. However, a recent clinical study using adjuvant mRNA vaccination in patients with pancreatic cancer identified an enrichment of nonresponders in patients who had their spleens removed during debulking surgery (*52*). Like us, the authors speculated that "optimal" antigen restimulation in the spleen might be associated with better therapeutic responses. Nonetheless, it remains unknown whether similar patterns of differentiation also occur in other lymphoid tissues, such as nondraining, distal lymph nodes, that may provide low but nonzero levels of antigen that support the differentiation of intermediate clonotypes. These studies might be particularly interesting in models of metastasis.

Together, our data highlight a previously unappreciated role for the spleen in coordinating the differentiation of tumor-reactive CD8$^+$ T cells as they respond to ICB. The splenic intermediate 1 phenotype that we identified comprised tumor-reactive CD8$^+$ T cells that expanded upon ICB treatment and gave rise to a majority of tumor-infiltrating clonotypes, suggesting that it is a crucial part of the antitumor immune response. This study provides mechanistic insight into ICB responses and will inform future studies of antitumor immune responses.

MATERIALS AND METHODS

Study design

Here, we used paired scRNA-seq and TCR sequencing to profile the endogenous, tumor-reactive T cells isolated from tumors, TdLNs, and spleens of mice treated with ICB to identify the transcriptional T cell states that maximally respond to ICB and the anatomic location they reside in. We functionally validated our findings using adoptive T cell transfer approaches and multiparameter flow cytometry.

ICB treatment

Mice were injected intraperitoneally with anti–CTLA-4 (clone UC10-4F10–11, Bio X Cell) and anti–PD-L1 (clone 10F.9G2, Bio X Cell) antibodies on days 7, 10, 13, and 16 after tumor inoculation for tumor outgrowth studies or on days 7 and 10 after tumor inoculation for day 14 analyses. Each mouse received 100 μg of each antibody per treatment.

2C T cell adoptive transfer

Spleens and inguinal lymph nodes (iLNs) of 2C RAG2$^{-/-}$CD45.1^{+} mice were dissected and made into single-cell suspensions as described above. Approximately 1 million cells were transferred to KP.SIY tumor–bearing mice 7 days after tumor inoculation. Recipient CD45.2^{+} animals were euthanized and analyzed 3 days after 2C T cell transfer. For transfers into secondary recipients, 2C T cells were transferred into primary recipients as described above. Three days after adoptive transfer, the tumor-draining iLNs or spleens of recipient mice were isolated, and CD8^{+} T cells were enriched with the Miltenyi CD8^{+} T cell isolation kit. Congenically marked CD45.1^{+} 2C T cells were then isolated from the CD8^{+} T cells using fluorescence-activated cell sorting, and 50,000 2C T cells were transferred intravenously into secondary recipient C57BL/6 mice bearing day 7 flank KP.SIY tumors. Additional serial transfer experiments were conducted by transferring isolated 50,000 2C T cells (as described above) into secondary C57BL/6 recipient mice with day 7 KP flank tumors and into secondary Batf3$^{-/-}$ recipient mice with day 7 KP.SIY flank tumors. Secondary recipients received ICB 1 and 3 days after adoptive transfer of in vivo–primed 2C T cells. TdLNs, spleens, and tumors from secondary recipients were analyzed 7 days after adoptive transfer of in vivo–primed 2C T cells.

In vivo antigen delivery

C57BL/6 splenocytes were isolated as described above, then ACK lysed, washed, and pulsed in complete medium for 1 hour at 37°C with 0.2 μM SIY peptide. SIY-pulsed splenocytes (20×10^6) were washed and injected intravenously into KP.SIY tumor–bearing mice on days 4, 6, and 9 after tumor inoculation. During this experiment, some mice were also treated with ICB on days 7 and 10 after tumor inoculation. Mice were analyzed on day 14 after tumor inoculation.

scRNA-seq with Seq-Well

Sorted cells were then processed for scRNA-seq using the Seq-Well platform with second-strand chemistry, as previously described (*53*, *54*). Whole-transcriptome libraries were barcoded and amplified using the Nextera XT kit (Illumina) and were sequenced on a Novaseq 6000 (Illumina). Hashtag oligo libraries were amplified as described previously and were sequenced on a Nextseq 550 (*34*). Whole-transcriptome libraries were sequenced to a median depth of >80,000 reads per cell recovered. Cell hashing libraries were sequenced to a medium depth of >3000 reads per cell recovered.

Processing of cell hashing data

Cell hashing data were aligned to hashtag oligo (HTO) barcodes using CITE-seq-Count v1.4.2. First, cells receiving fewer than five total HTO counts were classified as negatives. Downstream deconvolution of the hash-tag barcodes and analysis was conducted as previously described (*8*). Thresholds calculated for each sample were manually inspected and adjusted if necessary. Cells marked as doublets or negatives by this procedure were excluded from downstream analysis.

Processing of scRNA-seq data

Raw read processing of scRNA-seq reads was performed as previously described (*55*). Briefly, reads were aligned to the mm10 reference genome and collapsed by cell barcode and unique molecular identifier (UMI). Then, cells with fewer than 300 unique genes detected or with greater than 25% mitochondrial gene counts and genes detected in fewer than five cells were filtered out. Cell cycle scores for individual cells were computed using the CellCycleScoring function in Seurat. Data were then integrated by batch using Seurat v4.1.1 (*55*). The ScaleData function was used to regress out the number of RNA features in each cell, S and G_2-M cell cycle scores, and fraction of mitochondrial gene expression. The number of principal components used for visualization was determined by assessment of the elbow plot, and two-dimensional embeddings were generated using UMAP. Clusters were identified using Louvain clustering, as implemented in the FindClusters function in Seurat. Differentially expressed gene analysis was performed for each cluster and between indicated cell populations using the FindMarkers function. Data were iteratively reclustered to remove clusters with gene expression consistent with naïve T cells, monocytes, and NK cells. Label transfer of cluster labels onto proliferating cell populations was performed using the FindTransferAnchors and TransferData functions in Seurat (*55*).

Paired single-cell TCR sequencing and analysis

Paired TCR sequencing and read alignment was performed as described previously (*56*). In summary, TCR transcripts using biotinylated *Tcrb* and *Tcra* probes and magnetic streptavidin beads were enriched from the whole transcriptome amplification product from each single-cell library and further amplified using V-region primers and Nextera sequencing handles, and the resulting libraries were sequenced on an Illumina Novaseq 6000. Processing of raw sequencing reads was performed using the Immcantation software suite (*57*, *58*). First, the FilterSeq.py function was used to remove reads with an average quality score less than 25. Subsequent steps in CDR3 mapping were previously described (*8*). In brief, reads were sorted by cell barcode and UMI, and UMIs with fewer than 10 reads were discarded. Sets of sequences that comprised less than 30% of the sequences obtained for that UMI were discarded. BuildConsensus.py function and IgBlast (*59*) were used to determine consensus sequences, and sequences with no consensus sequence were discarded. The remaining TCR sequences were mapped to single-cell transcriptomes by matching cell barcodes. To define clonotypes of cells, we first segregated cells by mouse and unique *Tcrb* CDR3 junction nucleotide sequences. For each unique combination of mouse and CDR3β junction, we determined the most common TCRα sequence in cells with paired TCR recovery. We then imputed missing β chains from cells with recovery of only α chain by matching to these combinations of mouse, β chain, and α chain.

Statistical analysis

Statistical analyses were performed using GraphPad Prism (GraphPad) and R. All data are shown as means ± SEM. For flow cytometry and tumor outgrowth studies, statistical analyses were performed with the Mann-Whitney *U* test for comparisons of two groups, one-way analysis of variance (ANOVA) for comparisons among multiple

groups, or two-way ANOVA for multiple comparisons over time (unless explicitly stated otherwise), with $*P < 0.05$; $**P < 0.01$; $***P < 0.001$; and $****P < 0.0001$. For one-way and two-way ANOVAs, Šidák's or Tukey's multiple comparisons tests were used as posttests. For each experiment, two to four independent repeats were performed and combined; *n* numbers are indicated in figure captions. Statistical tests accompanying scRNA and single-cell TCR sequencing analyses are described in detail in figure captions.

Supplementary Materials

The PDF file includes:
Materials and Methods
Figs. S1 to S13
Table S1

Other Supplementary Material for this manuscript includes the following:
Data file S1
MDAR Reproducibility Checklist

REFERENCES AND NOTES

1. M. Karasarides, A. P. Cogdill, P. B. Robbins, M. Bowden, E. M. Burton, L. H. Butterfield, A. Cesano, C. Hammer, C. L. Haymaker, C. E. Horak, H. M. McGee, A. Monette, N. P. Rudqvist, C. N. Spencer, R. F. Sweis, B. G. Vincent, E. Wennerberg, J. Yuan, R. Zappasodi, V. M. H. Lucey, D. K. Wells, T. LaVallee, Hallmarks of resistance to immune-checkpoint inhibitors. *Cancer Immunol. Res.* **10**, 372–383 (2022).
2. D. Zehn, R. Thimme, E. Lugli, G. Pereira de Almeida, A. Oxenius, 'Stem-like' precursors are the fount to sustain persistent CD8$^+$ T cell responses. *Nat. Immunol.* **23**, 836–847 (2022).
3. A. Chow, K. Perica, C. A. Klebanoff, J. D. Wolchok, Clinical implications of T cell exhaustion for cancer immunotherapy. *Nat. Rev. Clin. Oncol.* **19**, 775–790 (2022).
4. A. Ribas, J. D. Wolchok, Cancer immunotherapy using checkpoint blockade. *Science* **359**, 1350–1355 (2018).
5. D. S. Chen, I. Mellman, Oncology meets immunology: The cancer-immunity cycle. *Immunity* **39**, 1–10 (2013).
6. M. B. Fuertes, A. K. Kacha, J. Kline, S.-R. Woo, D. M. Kranz, K. M. Murphy, T. F. Gajewski, Host type I IFN signals are required for antitumor CD8$^+$ T cell responses through CD8α$^+$ dendritic cells. *J. Exp. Med.* **208**, 2005–2016 (2011).
7. M. S. Diamond, M. Kinder, H. Matsushita, M. Mashayekhi, G. P. Dunn, J. M. Archambault, H. Lee, C. D. Arthur, J. M. White, U. Kalinke, K. M. Murphy, R. D. Schreiber, Type I interferon is selectively required by dendritic cells for immune rejection of tumors. *J. Exp. Med.* **208**, 1989–2003 (2011).
8. M. Zagorulya, L. Yim, D. M. Morgan, A. Edwards, E. Torres-Mejia, N. Momin, C. V. McCreery, I. L. Zamora, B. L. Horton, J. G. Fox, K. D. Wittrup, J. C. Love, S. Spranger, Tissue-specific abundance of interferon-gamma drives regulatory T cells to restrain DC1-mediated priming of cytotoxic T cells against lung cancer. *Immunity* **56**, 386–405.e10 (2023).
9. B. L. Horton, D. M. Morgan, N. Momin, M. Zagorulya, E. Torres-Mejia, V. Bhandarkar, K. D. Wittrup, J. C. Love, S. Spranger, Lack of CD8$^+$ T cell effector differentiation during priming mediates checkpoint blockade resistance in non-small cell lung cancer. *Sci. Immunol.* **6**, eabi8800 (2021).
10. C. Uyttenhove, J. Maryanski, T. Boon, Escape of mouse mastocytoma P815 after nearly complete rejection is due to antigen-loss variants rather than immunosuppression. *J. Exp. Med.* **157**, 1040–1052 (1983).
11. T. F. Gajewski, H. Schreiber, Y.-X. Fu, Innate and adaptive immune cells in the tumor microenvironment. *Nat. Immunol.* **14**, 1014–1022 (2013).
12. G. Oliveira, K. Stromhaug, S. Klaeger, T. Kula, D. T. Frederick, P. M. Le, J. Forman, T. Huang, S. Li, W. Zhang, Q. Xu, N. Cieri, K. R. Clauser, S. A. Shukla, D. Neuberg, S. Justesen, G. MacBeath, S. A. Carr, E. F. Fritsch, N. Hacohen, M. Sade-Feldman, K. J. Livak, G. M. Boland, P. A. Ott, D. B. Keskin, C. J. Wu, Phenotype, specificity and avidity of antitumour CD8$^+$ T cells in melanoma. *Nature* **596**, 119–125 (2021).
13. Y. Simoni, E. Becht, M. Fehlings, C. Y. Loh, S.-L. Koo, K. W. W. Teng, J. P. S. Yeong, R. Nahar, T. Zhang, H. Kared, K. Duan, N. Ang, M. Poidinger, Y. Y. Lee, A. Larbi, A. J. Khng, E. Tan, C. Fu, R. Mathew, M. Teo, W. T. Lim, C. K. Toh, B.-H. Ong, T. Koh, A. M. Hillmer, A. Takano, T. K. H. Lim, E. H. Tan, W. Zhai, D. S. W. Tan, I. B. Tan, E. W. Newell, Bystander CD8$^+$ T cells are abundant and phenotypically distinct in human tumour infiltrates. *Nature* **557**, 575–579 (2018).
14. A. O. Kamphorst, A. Wieland, T. Nasti, S. Yang, R. Zhang, D. L. Barber, B. T. Konieczny, C. Z. Daugherty, L. Koenig, K. Yu, G. L. Sica, A. H. Sharpe, G. J. Freeman, B. R. Blazar, L. A. Turka, T. K. Owonikoko, R. N. Pillai, S. S. Ramalingam, K. Araki, R. Ahmed, Rescue of exhausted CD8 T cells by PD-1-targeted therapies is CD28-dependent. *Science* **355**, 1423–1427 (2017).
15. E. Hui, J. Cheung, J. Zhu, X. Su, M. J. Taylor, H. A. Wallweber, D. K. Sasmal, J. Huang, J. M. Kim, I. Mellman, R. D. Vale, T cell costimulatory receptor CD28 is a primary target for PD-1-mediated inhibition. *Science* **355**, 1428–1433 (2017).
16. B. P. Fairfax, C. A. Taylor, R. A. Watson, I. Nassiri, S. Danielli, H. Fang, E. A. Mahé, R. Cooper, V. Woodcock, Z. Traill, M. Hussein, J. C. Knight, P. Klenerman, M. Payne, M. R. Middleton, Peripheral CD8$^+$ T cell characteristics associated with durable responses to immune checkpoint blockade in patients with metastatic melanoma. *Nat. Med.* **26**, 193–199 (2020).
17. D. T. Utzschneider, S. S. Gabriel, D. Chisanga, R. Gloury, P. M. Gubser, A. Vasanthakumar, W. Shi, A. Kallies, Early precursor T cells establish and propagate T cell exhaustion in chronic infection. *Nat. Immunol.* **21**, 1256–1266 (2020).
18. J.-C. Beltra, S. Manne, M. S. Abdel-Hakeem, M. Kurachi, J. R. Giles, Z. Chen, V. Casella, S. F. Ngiow, O. Khan, Y. J. Huang, P. Yan, K. Nzingha, W. Xu, R. K. Amaravadi, X. Xu, G. C. Karakousis, T. C. Mitchell, L. M. Schuchter, A. C. Huang, E. J. Wherry, Developmental relationships of four exhausted CD8$^+$ T cell subsets reveals underlying transcriptional and epigenetic landscape control mechanisms. *Immunity* **52**, 825–841.e8 (2020).
19. B. C. Miller, D. R. Sen, R. A. Abosy, K. Bi, Y. V. Virkud, M. W. LaFleur, K. B. Yates, A. Lako, K. Felt, G. S. Naik, M. Manos, E. Gjini, J. R. Kuchroo, J. J. Ishizuka, J. L. Collier, G. K. Griffin, S. Maleri, D. E. Comstock, S. A. Weiss, F. D. Brown, A. Panda, M. D. Zimmer, R. T. Manguso, F. S. Hodi, S. J. Rodig, A. H. Sharpe, W. N. Haining, Subsets of exhausted CD8$^+$ T cells differentially mediate tumor control and respond to checkpoint blockade. *Nat. Immunol.* **20**, 326–336 (2019).
20. Z. Chen, Z. Ji, S. F. Ngiow, S. Manne, Z. Cai, A. C. Huang, J. Johnson, R. P. Staupe, B. Bengsch, C. Xu, S. Yu, M. Kurachi, R. S. Herati, L. A. Vella, A. E. Baxter, J. E. Wu, O. Khan, J.-C. Beltra, J. R. Giles, E. Stelekati, L. M. McLane, C. W. Lau, X. Yang, S. L. Berger, G. Vahedi, H. Ji, E. J. Wherry, TCF-1-centered transcriptional network drives an effector versus exhausted CD8 T cell-fate decision. *Immunity* **51**, 840–855.e5 (2019).
21. M. A. Paley, D. C. Kroy, P. M. Odorizzi, J. B. Johnnidis, D. V. Dolfi, B. E. Barnett, E. K. Bikoff, E. J. Robertson, G. M. Lauer, S. L. Reiner, E. J. Wherry, Progenitor and terminal subsets of CD8$^+$ T cells cooperate to contain chronic viral infection. *Science* **338**, 1220–1225 (2012).
22. W. H. Hudson, J. Gensheimer, M. Hashimoto, A. Wieland, R. M. Valanparambil, P. Li, J.-X. Lin, B. T. Konieczny, S. J. Im, G. J. Freeman, W. J. Leonard, H. T. Kissick, R. Ahmed, Proliferating transitory T cells with an effector-like transcriptional signature emerge from PD-1$^+$ stem-like CD8$^+$ T cells during chronic infection. *Immunity* **51**, 1043–1058.e4 (2019).
23. S. J. Im, M. Hashimoto, M. Y. Gerner, J. Lee, H. T. Kissick, M. C. Burger, Q. Shan, J. S. Hale, J. Lee, T. H. Nasti, A. H. Sharpe, G. J. Freeman, R. N. Germain, H. I. Nakaya, H.-H. Xue, R. Ahmed, Defining CD8$^+$ T cells that provide the proliferative burst after PD-1 therapy. *Nature* **537**, 417–421 (2016).
24. Q. Huang, X. Wu, Z. Wang, X. Chen, L. Wang, Y. Lu, D. Xiong, Q. Liu, Y. Tian, H. Lin, J. Guo, S. Wen, W. Dong, X. Yang, Y. Yuan, Z. Yue, S. Lei, Q. Wu, L. Ran, L. Xie, Y. Wang, L. Gao, Q. Tian, X. Zhou, B. Sun, L. Xu, Z. Tang, L. Ye, The primordial differentiation of tumor-specific memory CD8$^+$ T cells as bona fide responders to PD-1/PD-L1 blockade in draining lymph nodes. *Cell* **185**, 4049–4066.e25 (2022).
25. D. M. Francis, M. P. Manspeaker, A. Schudel, L. F. Sestito, M. J. O'Melia, H. T. Kissick, B. P. Pollack, E. K. Waller, S. N. Thomas, Blockade of immune checkpoints in lymph nodes through locoregional delivery augments cancer immunotherapy. *Sci. Transl. Med.* **12**, eaay3575 (2020).
26. F. Dammeijer, M. van Gulijk, E. E. Mulder, M. Lukkes, L. Klaase, T. van den Bosch, M. van Nimwegen, S. P. Lau, K. Latupeirissa, S. Schetters, Y. van Kooyk, L. Boon, A. Moyaart, Y. M. Mueller, P. D. Katsikis, A. M. Eggermont, H. Vroman, R. Stadhouders, R. W. Hendriks, J. von der Thüsen, D. J. Grünhagen, C. Verhoef, T. van Hall, J. G. Aerts, The PD-1/PD-L1-checkpoint restrains T cell immunity in tumor-draining lymph nodes. *Cancer Cell* **38**, 685–700.e8 (2020).
27. I. Siddiqui, K. Schaeuble, V. Chennupati, S. A. Fuertes, S. Calderon-Copete, D. P. Ferreira, S. J. Carmona, L. Scarpellino, D. Gfeller, S. Pradervand, S. A. Luther, D. E. Speiser, W. Held, Intratumoral Tcf1$^+$PD-1$^+$CD8$^+$ T cells with stem-like properties promote tumor control in response to vaccination and checkpoint blockade immunotherapy. *Immunity* **50**, 195–211.e10 (2019).
28. C. S. Jansen, N. Prokhnevska, V. A. Master, M. G. Sanda, J. W. Carlisle, M. A. Bilen, M. Cardenas, S. Wilkinson, R. Lake, A. G. Sowalsky, R. M. Valanparambil, W. H. Hudson, D. McGuire, K. Melnick, A. I. Khan, K. Kim, Y. M. Chang, A. Kim, C. P. Filson, M. Alemozaffar, A. O. Osunkoya, P. Mullane, C. Ellis, R. Akondy, S. J. Im, A. O. Kamphorst, A. Reyes, Y. Liu, H. Kissick, An intra-tumoral niche maintains and differentiates stem-like CD8 T cells. *Nature* **576**, 465–470 (2019).
29. T. D. Wu, S. Madireddi, P. E. de Almeida, R. Banchereau, Y.-J. J. Chen, A. S. Chitre, E. Y. Chiang, H. Iftikhar, W. E. O'Gorman, A. Au-Yeung, C. Takahashi, L. D. Goldstein, C. Poon, S. Keerthivasan, D. E. de Almeida Nagata, X. Du, H.-M. Lee, K. L. Banta, S. Mariathasan, M. D. Thakur, M. A. Huseni, M. Ballinger, I. Estay, P. Caplazi, Z. Modrusan, L. Delamarre, I. Mellman, R. Bourgon, J. L. Grogan, Peripheral T cell expansion predicts tumour infiltration and clinical response. *Nature* **579**, 274–278 (2020).
30. A. O. Kamphorst, R. N. Pillai, S. Yang, T. H. Nasti, R. S. Akondy, A. Wieland, G. L. Sica, K. Yu, L. Koenig, N. T. Patel, M. Behera, H. Wu, M. M. Causland, Z. Chen, C. Zhang, F. R. Khuri,

T. K. Owonikoko, R. Ahmed, S. S. Ramalingam, Proliferation of PD-1+ CD8 T cells in peripheral blood after PD-1-targeted therapy in lung cancer patients. *Proc. Natl. Acad. Sci. U.S.A.* **114**, 4993–4998 (2017).
31. A. C. Huang, M. A. Postow, R. J. Orlowski, R. Mick, B. Bengsch, S. Manne, W. Xu, S. Harmon, J. R. Giles, B. Wenz, M. Adamow, D. Kuk, K. S. Panageas, C. Carrera, P. Wong, F. Quagliarello, B. Wubbenhorst, K. D'Andrea, K. E. Pauken, R. S. Herati, R. P. Staupe, J. M. Schenkel, S. M. Gettigan, S. Kothari, S. M. George, R. H. Vonderheide, R. K. Amaravadi, G. C. Karakousis, L. M. Schuchter, X. Xu, K. L. Nathanson, J. D. Wolchok, T. C. Gangadhar, E. J. Wherry, T-cell invigoration to tumour burden ratio associated with anti-PD-1 response. *Nature* **545**, 60–65 (2017).
32. J. R. Giles, S. F. Ngiow, S. Manne, A. E. Baxter, O. Khan, P. Wang, R. Staupe, M. S. Abdel-Hakeem, H. Huang, D. Mathew, M. M. Painter, J. E. Wu, Y. J. Huang, R. R. Goel, P. K. Yan, G. C. Karakousis, X. Xu, T. C. Mitchell, A. C. Huang, E. J. Wherry, Shared and distinct biological circuits in effector, memory and exhausted CD8$^+$ T cells revealed by temporal single-cell transcriptomics and epigenetics. *Nat. Immunol.* **23**, 1600–1613 (2022).
33. B. Daniel, K. E. Yost, S. Hsiung, K. Sandor, Y. Xia, Y. Qi, K. J. Hiam-Galvez, M. Black, C. J. Raposo, Q. Shi, S. L. Meier, J. A. Belk, J. R. Giles, E. J. Wherry, H. Y. Chang, T. Egawa, A. T. Satpathy, Divergent clonal differentiation trajectories of T cell exhaustion. *Nat. Immunol.* **23**, 1614–1627 (2022).
34. M. Stoeckius, S. Zheng, B. Houck-Loomis, S. Hao, B. Z. Yeung, W. M. Mauck III, P. Smibert, R. Satija, Cell Hashing with barcoded antibodies enables multiplexing and doublet detection for single cell genomics. *Genome Biol.* **19**, 224 (2018).
35. M. Xia, S. Hu, Y. Fu, W. Jin, Q. Yi, Y. Matsui, J. Yang, M. A. McDowell, S. Sarkar, V. Kalia, N. Xiong, CCR10 regulates balanced maintenance and function of resident regulatory and effector T cells to promote immune homeostasis in the skin. *J. Allergy Clin. Immunol.* **134**, 634–644.e10 (2014).
36. L. Kok, F. E. Dijkgraaf, J. Urbanus, K. Bresser, D. W. Vredevoogd, R. F. Cardoso, L. Perié, J. B. Beltman, T. N. Schumacher, A committed tissue-resident memory T cell precursor within the circulating CD8$^+$ effector T cell pool. *J. Exp. Med.* **217**, e20191711 (2020).
37. M. L. Broz, M. Binnewies, B. Boldajipour, A. E. Nelson, J. L. Pollack, D. J. Erle, A. Barczak, M. D. Rosenblum, A. Daud, D. L. Barber, S. Amigorena, L. J. Van't Veer, A. I. Sperling, D. M. Wolf, M. F. Krummel, Dissecting the tumor myeloid compartment reveals rare activating antigen-presenting cells critical for T cell immunity. *Cancer Cell* **26**, 638–652 (2014).
38. S. Spranger, D. Dai, B. Horton, T. F. Gajewski, Tumor-residing Batf3 dendritic cells are required for effector T cell trafficking and adoptive T cell therapy. *Cancer Cell* **31**, 711–723. e4 (2017).
39. P. Meiser, M. A. Knolle, A. Hirschberger, G. P. de Almeida, F. Bayerl, S. Lacher, A.-M. Pedde, S. Flommersfeld, J. Hönninger, L. Stark, F. Stögbauer, M. Anton, M. Wirth, D. Wohlleber, K. Steiger, V. R. Buchholz, B. Wollenberg, C. E. Zielinski, R. Braren, D. Rueckert, P. A. Knolle, G. Kaissis, J. P. Böttcher, A distinct stimulatory cDC1 subpopulation amplifies CD8$^+$ T cell responses in tumors for protective anti-cancer immunity. *Cancer Cell* **41**, 1498–1515.e10 (2023).
40. E. W. Roberts, M. L. Broz, M. Binnewies, M. B. Headley, A. E. Nelson, D. M. Wolf, T. Kaisho, D. Bogunovic, N. Bhardwaj, M. F. Krummel, Critical role for CD103$^+$/CD141$^+$ dendritic cells bearing CCR7 for tumor antigen trafficking and priming of t cell immunity in melanoma. *Cancer Cell* **30**, 324–336 (2016).
41. X. Chen, B. W. MacNabb, B. Flood, B. R. Blazar, J. Kline, Divergent fates of antigen-specific CD8$^+$ T cell clones in mice with acute leukemia. *Cell Rep.* **37**, 109991 (2021).
42. B. W. MacNabb, S. Tumuluru, X. Chen, J. Godfrey, D. N. Kasal, J. Yu, M. L. M. Jongsma, R. M. Spaapen, D. E. Kline, J. Kline, Dendritic cells can prime anti-tumor CD8$^+$ T cell responses through major histocompatibility complex cross-dressing. *Immunity* **55**, 982–997.e8 (2022).
43. L. Zheng, S. Qin, W. Si, A. Wang, B. Xing, R. Gao, X. Ren, L. Wang, X. Wu, J. Zhang, N. Wu, N. Zhang, H. Zheng, H. Ouyang, K. Chen, Z. Bu, X. Hu, J. Ji, Z. Zhang, Pan-cancer single-cell landscape of tumor-infiltrating T cells. *Science* **374**, abe6474 (2021).
44. R. Zander, D. Schauder, G. Xin, C. Nguyen, X. Wu, A. Zajac, W. Cui, CD4$^+$ T cell help is required for the formation of a cytolytic CD8$^+$ T cell subset that protects against chronic infection and cancer. *Immunity* **51**, 1028–1042.e4 (2019).
45. N. Prokhnevska, M. A. Cardenas, R. M. Valanparambil, E. Sobierajska, B. G. Barwick, C. Jansen, A. R. Moon, P. Gregorova, L. delBalzo, R. Greenwald, M. A. Bilen, M. Alemozaffar, S. Joshi, C. Cimmino, C. Larsen, V. Master, M. Sanda, H. Kissick, CD8$^+$ T cell activation in cancer comprises an initial activation phase in lymph nodes followed by effector differentiation within the tumor. *Immunity* **56**, 107–124.e5 (2023).
46. C. Gerlach, E. A. Moseman, S. M. Loughhead, D. Alvarez, A. J. Zwijnenburg, L. Waanders, R. Garg, J. C. de la Torre, U. H. von Andrian, The chemokine receptor CX3CR1 defines three antigen-experienced CD8 T cell subsets with distinct roles in immune surveillance and homeostasis. *Immunity* **45**, 1270–1284 (2016).
47. M. E. Mikucki, D. T. Fisher, J. Matsuzaki, J. J. Skitzki, N. B. Gaulin, J. B. Muhitch, A. W. Ku, J. G. Frelinger, K. Odunsi, T. F. Gajewski, A. D. Luster, S. S. Evans, Non-redundant requirement for CXCR3 signalling during tumoricidal T-cell trafficking across tumour vascular checkpoints. *Nat. Commun.* **6**, 7458 (2015).
48. T. Yamauchi, T. Hoki, T. Oba, R. Kajihara, K. Attwood, X. Cao, F. Ito, CD40 and CD80/86 signaling in cDC1s mediate effective neoantigen vaccination and generation of antigen-specific CX3CR1$^+$ CD8$^+$ T cells. *Cancer Immunol. Immunother.* **71**, 137–151 (2022).
49. T. Yamauchi, T. Hoki, T. Oba, H. Saito, K. Attwood, M. S. Sabel, A. E. Chang, K. Odunsi, F. Ito, CX3CR1$^-$CD8$^+$ T cells are critical in antitumor efficacy but functionally suppressed in the tumor microenvironment. *JCI Insight* **5**, e133920 (2020).
50. A. L. Burrack, E. J. Spartz, M. R. Rollins, E. A. Miller, M. Firulyova, E. Cruz, M. F. Goldberg, I. X. Wang, H. Nanda, S. Shen, K. Zaitsev, I. M. Stromnes, Cxcr3 constrains pancreatic cancer dissemination through instructing T cell fate. *Cancer Immunol. Immunother.* **72**, 1461–1478 (2023).
51. T. Yamauchi, T. Hoki, T. Oba, V. Jain, H. Chen, K. Attwood, S. Battaglia, S. George, G. Chatta, I. Puzanov, C. Morrison, K. Odunsi, B. H. Segal, G. K. Dy, M. S. Ernstoff, F. Ito, T-cell CX3CR1 expression as a dynamic blood-based biomarker of response to immune checkpoint inhibitors. *Nat. Commun.* **12**, 1402 (2021).
52. L. A. Rojas, Z. Sethna, K. C. Soares, C. Olcese, N. Pang, E. Patterson, J. Lihm, N. Ceglia, P. Guasp, A. Chu, R. Yu, A. K. Chandra, T. Waters, J. Ruan, M. Amisaki, A. Zebboudj, Z. Odgerel, G. Payne, E. Derhovanessian, F. Müller, I. Rhee, M. Yadav, A. Dobrin, M. Sadelain, M. Łuksza, N. Cohen, L. Tang, O. Basturk, M. Gönen, S. Katz, R. K. Do, A. S. Epstein, P. Momtaz, W. Park, R. Sugarman, A. M. Varghese, E. Won, A. Desai, A. C. Wei, M. I. D'Angelica, T. P. Kingham, I. Mellman, T. Merghoub, J. D. Wolchok, U. Sahin, Ö. Türeci, B. D. Greenbaum, W. R. Jarnagin, J. Drebin, E. M. O'Reilly, V. P. Balachandran, Personalized RNA neoantigen vaccines stimulate T cells in pancreatic cancer. *Nature* **618**, 144–150 (2023).
53. T. M. Gierahn, M. H. Wadsworth II, T. K. Hughes, B. D. Bryson, A. Butler, R. Satija, S. Fortune, J. C. Love, A. K. Shalek, Seq-Well: Portable, low-cost RNA sequencing of single cells at high throughput. *Nat. Methods* **14**, 395–398 (2017).
54. T. K. Hughes, M. H. Wadsworth II, T. M. Gierahn, T. Do, D. Weiss, P. R. Andrade, F. Ma, B. J. de Andrade Silva, S. Shao, L. C. Tsoi, J. Ordovas-Montanes, J. E. Gudjonsson, R. L. Modlin, J. C. Love, A. K. Shalek, Second-strand synthesis-based massively parallel scRNA-seq reveals cellular states and molecular features of human inflammatory skin pathologies. *Immunity* **53**, 878–894.e7 (2020).
55. E. Z. Macosko, A. Basu, R. Satija, J. Nemesh, K. Shekhar, M. Goldman, I. Tirosh, A. R. Bialas, N. Kamitaki, E. M. Martersteck, J. J. Trombetta, D. A. Weitz, J. R. Sanes, A. K. Shalek, A. Regev, S. A. McCarroll, Highly parallel genome-wide expression profiling of individual cells using nanoliter droplets. *Cell* **161**, 1202–1214 (2015).
56. A. A. Tu, T. M. Gierahn, B. Monian, D. M. Morgan, N. K. Mehta, B. Ruiter, W. G. Shreffler, A. K. Shalek, J. C. Love, TCR sequencing paired with massively parallel 3' RNA-seq reveals clonotypic T cell signatures. *Nat. Immunol.* **20**, 1692–1699 (2019).
57. J. A. Vander Heiden, G. Yaari, M. Uduman, J. N. H. Stern, K. C. O'Connor, D. A. Hafler, F. Vigneault, S. H. Kleinstein, pRESTO: A toolkit for processing high-throughput sequencing raw reads of lymphocyte receptor repertoires. *Bioinformatics* **30**, 1930–1932 (2014).
58. N. T. Gupta, J. A. Vander Heiden, M. Uduman, D. Gadala-Maria, G. Yaari, S. H. Kleinstein, Change-O: A toolkit for analyzing large-scale B cell immunoglobulin repertoire sequencing data. *Bioinformatics* **31**, 3356–3358 (2015).
59. J. Ye, N. Ma, T. L. Madden, J. M. Ostell, IgBLAST: An immunoglobulin variable domain sequence analysis tool. *Nucleic Acids Res.* **41**, W34–W40 (2013).
60. J. R. Giles, S. Manne, E. Freilich, D. A. Oldridge, A. E. Baxter, S. George, Z. Chen, H. Huang, L. Chilukuri, M. Carberry, L. Giles, N.-P. P. Weng, R. M. Young, C. H. June, L. M. Schuchter, R. K. Amaravadi, X. Xu, G. C. Karakousis, T. C. Mitchell, A. C. Huang, J. Shi, E. J. Wherry, Human epigenetic and transcriptional T cell differentiation atlas for identifying functional T cell-specific enhancers. *Immunity* **55**, 557–574.e7 (2022).

Acknowledgments: We would like to extend a special acknowledgement of the significant contributions of Brendan L. Horton to the field of tumor immunology during his research career, which was too short. Brendan was a born scientist with the desire to understand the unknowns, and he pursued his desire in an unparalleled collegial and collaborative way. He will be forever missed as a scientist, colleague, and friend. We would like to thank M. Duquette for mouse colony maintenance and P. Thompson and J. Teixeira for administrative support. We thank the Koch Institute's Robert A. Swanson (1969) Biotechnology Center for providing core services. **Funding:** This work was supported by NIH cancer core grant P30 CA014051-49, a postdoctoral fellowship from the Ludwig Center at MIT's Koch Institute for Integrative Cancer Research, a Pew-Stewart scholarship, and the NCI-funded grant 1R37CA273819-01A1. **Author contributions:** D.M.M.: designing research studies, conducting experiments, acquiring data, analyzing data, writing the manuscript, and revising the manuscript. B.L.H.: designing research studies, conducting experiments, acquiring data, analyzing data, and writing the manuscript. V.B.: designing research studies, conducting experiments, acquiring data, analyzing data, and revising the manuscript. R.V.: conducting experiments, acquiring data, analyzing data. T.D.:

conducting experiments, acquiring data, and analyzing data. M.Z.: conducting experiments, acquiring data, and analyzing data. J.C.L.: securing research support, designing research studies, providing reagents, and writing the manuscript. S.S.: securing research support, designing research studies, writing the manuscript, and overseeing the study. **Competing interests:** J.C.L. is a cofounder and adviser to Honeycomb Biotechnologies. S.S. is an SAB member for Related Sciences, Arcus Biosciences, Ankyra Therapeutics, and Repertoire Immune Medicines. S.S. is a cofounder of Danger Bio. S.S. is a consultant for TAKEDA and Merck and receives funding for unrelated projects from Leap Therapeutics and iTeos Therapeutics. J.C.L.'s and S.S.'s interests were reviewed and managed under MIT's policies for potential conflicts of interest. The other authors declare that they have no competing interests. **Data and materials availability:** Tabulated data underlying the figures are provided in data file S1. Single-cell transcriptome data from untreated flank tumors were previously published in GSE184388. All of the remaining sequencing data are also available on GEO, accession number GSE270050. Codes used to perform preprocessing and analysis of single-cell data are available at https://github.com/duncanmorgan/KPSpleen and are archived on Zenodo (10.5281/zenodo.12786217). All other data needed to evaluate the conclusions in the paper are present in the paper or the Supplementary Materials.

Submitted 19 April 2023
Resubmitted 11 May 2024
Accepted 15 August 2024
Published 13 September 2024
10.1126/sciimmunol.adi3487